

Fully Discrete Active Flux Method based on Transported Acoustic Increments for the Compressible Euler Equations^{*}

Karthik Duraisamy^a

^aDepartment of Aerospace Engineering, University of Michigan, Ann Arbor, MI, USA

ARTICLE INFO

Keywords:

Active Flux, Compressible flows, High order methods, Structure preservation

ABSTRACT

A fully discrete Active Flux method is proposed for the two-dimensional compressible Euler equations. The method builds on the evolution-operator formulation of multidimensional Active Flux proposed by Roe in which conservative cell averages are updated by unsplit flux quadrature while primitive point values are evolved by acoustic and advective subsolvers. This has recently been extended to the Euler equations by Barsukow, who developed an efficient approach by adding acoustic increments at the Eulerian target point. It is shown that, in a frozen linearized setting, this misses the leading symmetric advection–acoustic cross interaction. The proposed method instead reconstructs the acoustic increment as a cellwise Q2 field, using vertex, edge-midpoint, and cell-center acoustic increments, and evaluates this field at the convective foot of the target point. For constant frozen coefficients, the resulting point update reduces to the transported composition, eliminating the additive split defect and yielding the exact unsplit frozen evolution when the acoustic and advective generators commute. The resulting method preserves the exact locally linearized acoustic evolution operator of Barsukow, the compact stencil, and the conservative one-stage average update. Numerical experiments probe several facets of the numerical method. A mixed Fourier wave packet isolates the split error and shows third-order point accuracy for the transported update, compared with second-order behavior for the additive update. Isentropic vortex convection confirms third-order convergence for the full nonlinear scheme, reduced error constants, and an enlarged empirical CFL range. Nonlinear Gaussian acoustic pulse evolution demonstrates preservation of radial symmetry and near-third-order decay of the symmetry error. Low-Mach shear-layer tests show coherent vorticity evolution, ultra-low entropy dissipation, and absence of the coarse-grid secondary vortices seen in displayed DG/CG comparisons. Finally, a compressible under-resolved Kelvin–Helmholtz test demonstrates robust no-limiter evolution to late time with consistent entropy dissipation. Fourier diagnostics of the vertical-edge point operator support the observed improvements in acoustic phase and amplification behavior.


1. Introduction


Despite many advances in high order methods (Wang, Fidkowski, Abgrall, Bassi, Caraeni, Cary, Deconinck, Hartmann, Hillewaert, Huynh et al., 2013; Ferrer, Rubio, Ntoukas, Laskowski, Marino, Colombo, Mateo-Gabín, Marbona, de Lara, Huergo et al., 2023; Mani and Dorgan, 2023) over the past two decades, effective computation of compressible flows remains an outstanding challenge. This is particularly true when viewed via the lens of practical computations of complex problems such as high Reynolds number aerodynamics, radiation hydrodynamics where one cannot afford spatio-temporal resolutions corresponding to asymptotically convergent regimes. Thus, there is a need for accurate, robust and efficient numerical methods that preserve important flow features at coarse resolutions, while providing the order of accuracy with refinement of the discretization.

Roe (2025) reminds us that the fundamental questions concerning a numerical method for hyperbolic conservation laws are easy to state but rarely respected: what information should be used to find the solution?, and is that information being propagated through the right geometric channels? In one space dimension the question is benign: The exact domain of dependence is a segment, and standard upwinding can be made to coincide with it. In multiple dimensions, however, the exact domain of dependence is a Mach cone, the relevant signals propagate along a range of directions, and dimensionally split or one-dimensional Riemann-solver-based discretizations inevitably approximate this cone by anisotropic, axis-aligned proxies. Such schemes can be formally high-order in the dispersive sense yet, in Roe's

^{*}This document is the result of a research project funded by Los Alamos National Laboratory.

^{*}Corresponding author

 kdur@umich.edu (K. Duraisamy)

 caslab.engin.umich.edu (K. Duraisamy)

ORCID(s): 0000-0002-3519-8147 (K. Duraisamy)

diagnosis, deficient in *bandwidth* (Roe, 2021): they fail to transmit short-wavelength multi-dimensional information cleanly, regardless of formal order. A genuinely satisfactory numerical method should therefore (i) carry a *compact, symmetric* stencil whose discrete domain of dependence approximates the actual Mach cone rather than its axis-aligned envelope; (ii) propagate information along the true multi-dimensional characteristics of the system rather than along the coordinate axes (Roe, 2017); (iii) be *fully discrete* and *single stage*, so as not to import the ad-hoc damping and effective stencil enlargement of multistage time integrators; and (iv) deliver these properties uniformly across regimes, without recourse to solution-dependent fixes such as low-Mach preconditioning (Guillard and Viozat, 1999; Dellacherie, 2010), asymptotic-preserving patches, or limiter machinery tuned per regime. A scheme that propagates the genuinely multi-dimensional signals correctly, in particular, the divergence-free, vorticity, and stationarity content of the linear acoustic system, inherits the correct low-Mach behaviour as a by-product, rather than as a fix.

The Active Flux method is one of the few CFD frameworks designed from the outset around all four of the principles above. It originates in the seminal ‘Scheme V’ of van Leer (1977), which proposed a method for one-dimensional conservation laws, carrying alongside the cell average, an additional pointwise degree of freedom and updates it by tracing the foot of the characteristic. Around 15 years ago, Eymann and Roe (2011, 2013) revived this idea and extended the construction to nonlinear systems and to genuinely two-dimensional linear problems. The defining feature of the framework is the simultaneous storage of conservative cell averages *and* pointwise primitive degrees of freedom located on cell interfaces (vertices and edge midpoints), tied together by a globally continuous reconstruction. Two distinct mechanisms operate on these unknowns: a conservative average update, which uses the point values directly as quadrature data for the unsplit fluxes and therefore requires no Riemann solver; and a non-conservative point update, which is responsible for upwinding and is naturally formulated as a (possibly approximate) evolution operator. When that evolution operator is exact, the resulting method is one-stage, compact, stable up to $CFL = 1$, and transports information genuinely multi-dimensionally. The downstream consequences are remarkable: on Cartesian grids the linearized Active Flux method is provably stationarity- and vorticity-preserving and exhibits the correct low-Mach limit *without* any preconditioning (Barsukow, Hohm, Klingenberg and Roe, 2019; Barsukow, 2021b), while the third-order theory (in 1D problems) developed by Barsukow (2021a) closes the gap to high-order accuracy on nonlinear systems without sacrificing compactness.

For systems of non-linear conservation laws in more than one space dimension, however, the construction of a sufficiently accurate *pointwise* evolution operator remains the central technical difficulty, and the literature pursues two distinct approaches. One line of work, semi-discrete in time, replaces the evolution operator with a non-standard finite-difference reconstruction of the time derivative and integrates the resulting ODE with a Runge-Kutta method (Abgrall and Barsukow, 2023; Abgrall, Barsukow and Klingenberg, 2025). The approach is general but reintroduces multistage diffusion and forces small CFL numbers, sacrificing the very compactness and one-stage purity that motivated Active Flux. The complementary line adheres to the original van Leer-Roe ideals and seeks an evolution operator. The doctoral theses of Fan (2017) and Maeng (2017) at the University of Michigan pursue this theme by separately treating the acoustic and advective components of the multi-dimensional Euler system; an extended Lax-Wendroff / Cauchy-Kowalevskaya construction in the same vein is compared with discontinuous Galerkin methods in (Roe, Maeng and Fan, 2018). The acoustic part rests on a result of Barsukow and Klingenberg (2022), who derived the exact evolution operator for the linearized acoustic equations on a general class of (possibly non-smooth) initial data, exposing the truly multi-dimensional structure of acoustic propagation and providing a path for genuinely multi-dimensional Godunov and Active Flux schemes. A non-split bicharacteristic construction has recently been pursued by Chudzik, Helzel and Lukáčová-Medvid’ová (2024) and Chudzik, Helzel and Porfetye (2025), and presents an interesting direction.

These ingredients have very recently been assembled by Barsukow (2025a) into a fully discrete Active Flux method for the two-dimensional compressible Euler equations. The point values are evolved by an *additive* operator split: at every node, the acoustic subsystem is locally linearised about the frozen primitive state and advanced by the exact evolution operator of Barsukow and Klingenberg (2022), while the nonlinear advection subsystem is advanced by a third-order foot-point iteration. Cell averages are then updated conservatively by space-time Simpson quadrature of the unsplit Euler fluxes. The scheme is one-stage, compact, and inherits the structure-preserving properties of its acoustic ancestor, providing a clean reference implementation of evolution-operator-based multi-dimensional Active Flux for the Euler system.

The contribution of this paper is a fully discrete Active Flux scheme that retains key elements of Barsukow (2025a), but replaces the additive composition by a *transported acoustic-increment* modification of the point-value update. The acoustic increment field is reconstructed across each cell as a Q_2 polynomial, using the increments naturally available at vertices and edge midpoints together with a centre-cell increment obtained by a full-disk acoustic update;

this Q_2 field is then evaluated at the convective foot P_f , rather than added at the Eulerian node P as in Barsukow (2025a). In a frozen linear setting, it is shown that this converts the additive split into a transported composition that eliminates the leading $\mathcal{O}(\tau^2)$ piece of the advection/acoustic cross-term defect. Numerical experiments on the isentropic vortex, planar acoustic propagation, and shear-layer evolution show markedly improved resolution of vortex and shear structures, with a larger stable CFL range. We provide Fourier analysis of the improved point schemes and also report on unsuccessful, more intrusive variants and identify the minimal-intervention modification that remains compatible with its structure-preserving properties.

The remainder of the paper is organised as follows. Section 2 details the setup of the Active Flux infrastructure in two dimensions. Section 3 reviews the fully discrete Barsukow scheme and quantifies the cross-term defect of its additive split. Section 4 introduces the transported-increment method, the Q_2 reconstruction of the acoustic increment, and an operator-level analysis of the modified split. Subsequent sections report numerical experiments on the isentropic vortex, planar acoustics, and shear flow, together with a Fourier analysis that corroborates the observed behaviour at the level of the frozen acoustics. The explicit form of the acoustic update at a vertical edge node is provided in the appendix.

2. Active Flux Infrastructure in 2D

We consider the two-dimensional compressible Euler equations

$$\partial_t \mathbf{U} + \partial_x \mathbf{F}(\mathbf{U}) + \partial_y \mathbf{G}(\mathbf{U}) = 0, \quad \mathbf{U} = (\rho, \rho u, \rho v, E)^T, \quad (1)$$

with ideal-gas closure

$$E = \frac{p}{\gamma - 1} + \frac{1}{2} \rho (u^2 + v^2). \quad (2)$$

The corresponding primitive state is $\mathbf{W} = (\rho, u, v, p)^T$, $c^2 = \gamma p / \rho$.

The computational grid is Cartesian and periodic, with equal spacing $\Delta x = \Delta y = h$. Cells are denoted $C_{ij} = [x_i, x_{i+1}] \times [y_j, y_{j+1}]$, with cell center $(x_{i+1/2}, y_{j+1/2})$. This work uses the following convention: conservative variables are used for cell averages, primitive variables are used for point values and reconstruction. This is the choice made in Barsukow's multidimensional Euler Active Flux method, because it substantially simplifies the acoustic evolution operator while the average update remains conservative (Barsukow, 2025a).

The degrees of freedom are:

- conservative cell averages $\bar{\mathbf{U}}_{ij} \approx \frac{1}{|C_{ij}|} \int_{C_{ij}} \mathbf{U}(x, y, t) dx dy$;
- primitive point values at vertices, $\mathbf{W}_{ij}^V \approx \mathbf{W}(x_i, y_j, t)$;
- primitive point values at vertical-edge midpoints, $\mathbf{W}_{ij}^{E_v} \approx \mathbf{W}(x_i, y_{j+1/2}, t)$;
- primitive point values at horizontal-edge midpoints, $\mathbf{W}_{ij}^{E_h} \approx \mathbf{W}(x_{i+1/2}, y_j, t)$.

Within each cell, the reconstruction is a tensor-product quadratic polynomial, i.e. a Q_2 or biquadratic polynomial. Eight of its nine nodal values are already known from the point values on the boundary. The ninth node is the cell-center value. It is obtained by inverting the tensor-product Simpson rule in conservative variables.

Let \mathbf{U}_c denote the unknown conservative cell-center node. Let the four corner conservative values and four edge-midpoint conservative values be obtained by converting the primitive point values to conservative variables. The tensor-product Simpson average is

$$\bar{\mathbf{U}}_{ij} = \frac{1}{36} \sum_{\text{corners}} \mathbf{U} + \frac{1}{9} \sum_{\text{edge mids}} \mathbf{U} + \frac{4}{9} \mathbf{U}_c. \quad (3)$$

Thus

$$\mathbf{U}_c = \frac{9}{4} \left[\bar{\mathbf{U}}_{ij} - \frac{1}{36} \sum_{\text{corners}} \mathbf{U} - \frac{1}{9} \sum_{\text{edge mids}} \mathbf{U} \right]. \quad (4)$$

Finally U_c is converted back to a primitive center node W_c . The primitive Q_2 reconstruction in cell C_{ij} is then

$$W_{ij}^{\text{recon}}(\xi, \eta) \triangleq \sum_{a=-1}^1 \sum_{b=-1}^1 \ell_a(\xi) \ell_b(\eta) W_{ab}^{ij}, \quad -1 \leq \xi, \eta \leq 1, \quad (5)$$

where $\ell_{-1}, \ell_0, \ell_1$ are the Lagrange polynomials at $-1, 0, 1$, and W_{ab}^{ij} are the nine primitive nodal values in the cell. Because each edge restriction is a one-dimensional quadratic interpolating the same three edge point values from either adjacent cell, the reconstruction is continuous across cell interfaces. This is the characteristic Active Flux feature: the reconstruction is globally continuous, but the cell average remains a conservative degree of freedom (Roe, 2017).

3. Fully discrete Active Flux Scheme

In the fully discrete method of Barsukow (2025a), the point values are evolved by an approximate evolution operator built from an acoustic/advection decomposition of primitive Euler. The average update is then performed conservatively using space-time Simpson quadrature of the unsplit Euler fluxes.

3.1. Acoustic/advection split

As proposed by Roe and his students (Fan, 2017; Maeng, 2017), and further developed more recently (Barsukow and Klingenberg, 2022; Barsukow, 2025a) the primitive Euler equations are split into an acoustic part and an advection part. The acoustic part is

$$\rho_t + \rho \nabla \cdot \mathbf{u} \triangleq 0, \quad (6)$$

$$\mathbf{u}_t + \frac{1}{\rho} \nabla p \triangleq 0, \quad (7)$$

$$p_t + \rho c^2 \nabla \cdot \mathbf{u} \triangleq 0. \quad (8)$$

At each point value P , one freezes $\rho_0 \triangleq \rho^n(P)$, $c_0 \triangleq c^n(P)$, and introduces the acoustic scalar

$$\pi \triangleq \frac{p}{\rho_0 c_0}. \quad (9)$$

The locally linearized acoustic equations become

$$\mathbf{u}_t + c_0 \nabla \pi = 0, \quad (10)$$

$$\pi_t + c_0 \nabla \cdot \mathbf{u} = 0. \quad (11)$$

This linear acoustic system is solved using the exact acoustic evolution operator. In the Cartesian implementation, a vertex uses four quadrant wedges and an edge midpoint uses two half-plane wedges. The exact acoustic evolution is applied to the local Q_2 reconstruction in each adjacent wedge, and the contributions are summed. The paper's implementation pseudocode expresses this by precomputing polynomial-in- r evolution coefficients for monomials and wedge geometries, then contracting those coefficients with the runtime polynomial coefficients (Barsukow, 2025a).

We find that it is possible to obtain explicit and exact expressions for the velocity and pressure updates in terms of the nodal coefficients, thus offering good insight for analysis. The expression for the pressure update at the vertical face node is given in Appendix B, and exploited later for Fourier analysis.

The density is recovered from the frozen acoustic invariant $\partial_t(\rho c_0^2 - p) = 0$. If the acoustic solve returns p_{ac} , then

$$\rho_{\text{ac}} = \rho_0 + \frac{p_{\text{ac}} - p_0}{c_0^2}. \quad (12)$$

We denote the resulting acoustic point evolution by $S_{\text{ac}}(\tau)W^n(P)$. The advection part is $W_t + \mathbf{u}(W) \cdot \nabla W = 0$.

Barsukow uses a third-order footpoint rule for this nonlinear advection subsystem. For a target point P , the advection update is

$$S_{\text{adv}}(\tau)W^n(P) \triangleq W^n(P - \tau \mathbf{u}^n(P - \tau \mathbf{u}^n(P))). \quad (13)$$

This is the multidimensional nonlinear-advection analogue of a second Picard footpoint iteration. Barsukow proves the corresponding third-order statement for the nonlinear advection subsystem (Barsukow, 2025a).

Following this an additive point update (Barsukow, 2025a) is performed

$$\mathbf{W}_{\text{RB}}^{n+\tau}(P) \triangleq S_{\text{ac}}(\tau)\mathbf{W}^n(P) + S_{\text{adv}}(\tau)\mathbf{W}^n(P) - \mathbf{W}^n(P). \quad (14)$$

The update is deliberately simple. Both subsolvers act on the same time- n reconstruction. The cell average is not updated by either split subproblem; instead, after point values have been evolved to $t^n + \Delta t/2$ and $t^n + \Delta t$, the conservative average update uses the unsplit Euler fluxes.

Barsukow's paper notes that the reconstruction and quadratures are third order, and the nonlinear advection subsolver is third order, but the locally linearized acoustics and additive splitting are formally second order in time (Barsukow, 2025a).

For one full time step Δt , point values are computed at t^n , $t^{n+1/2}$, and t^{n+1} . Let $\hat{F}_{i,j}^m$ denote the spatial Simpson edge flux at time level $m \in \{0, 1/2, 1\}$ on the vertical edge $x = x_i$. Then the time-averaged edge flux is

$$\hat{F}_{i,j} = \frac{1}{6}\hat{F}_{i,j}^0 + \frac{4}{6}\hat{F}_{i,j}^{1/2} + \frac{1}{6}\hat{F}_{i,j}^1. \quad (15)$$

The cell average update is

$$\bar{U}_{ij}^{n+1} = \bar{U}_{ij}^n - \frac{\Delta t}{h}(\hat{F}_{i+1,j} - \hat{F}_{i,j}) - \frac{\Delta t}{h}(\hat{G}_{i,j+1} - \hat{G}_{i,j}). \quad (16)$$

This update is conservative because it is a flux-difference update in conservative variables.

Given the history and recent developments, we refer to this scheme as the Discrete Roe-Barsukow method when comparing to other techniques. The semi-discrete active flux method of Abgrall et al. (2025) is presented in the Appendix and will be used for comparisons.

3.2. Operator Error Analysis

Linearize the primitive variables about a uniform state $\mathbf{W}_0 \triangleq (\rho_0, u_0, v_0, p_0)^T$, $c_0^2 = \gamma p_0/\rho_0$. Write the perturbation as $\mathbf{w} = (\rho', u', v', p')^T$. The frozen linearized primitive Euler equations are

$$\rho'_t + u_0\rho'_x + v_0\rho'_y + \rho_0(u'_x + v'_y) = 0, \quad (17)$$

$$u'_t + u_0u'_x + v_0u'_y + \frac{1}{\rho_0}p'_x = 0, \quad (18)$$

$$v'_t + u_0v'_x + v_0v'_y + \frac{1}{\rho_0}p'_y = 0, \quad (19)$$

$$p'_t + u_0p'_x + v_0p'_y + \rho_0c_0^2(u'_x + v'_y) = 0. \quad (20)$$

Equivalently, $\partial_t\mathbf{w} = (A + C)\mathbf{w}$, where $A \triangleq -(u_0\partial_x + v_0\partial_y)I$ is the scalar advection generator and C is the frozen acoustic generator:

$$C\mathbf{w} \triangleq - \begin{pmatrix} \rho_0(u'_x + v'_y) \\ p'_x/\rho_0 \\ p'_y/\rho_0 \\ \rho_0c_0^2(u'_x + v'_y) \end{pmatrix}.$$

Let $S_{\text{ac}}(\tau)$ and $S_{\text{adv}}(\tau)$ denote the acoustic and advective subsolvers. Linearized about a uniform state, these are $S_{\text{ac}}(\tau) = e^{\tau C}$, $S_{\text{adv}}(\tau) = e^{\tau A}$. Barsukow's additive point update has the linearized form $E_B(\tau) = e^{\tau A} + e^{\tau C} - I$. Expanding in τ , $E_B(\tau) = I + \tau(A + C) + \frac{\tau^2}{2}(A^2 + C^2) + \frac{\tau^3}{6}(A^3 + C^3) + \mathcal{O}(\tau^4)$. The exact frozen unsplit evolution is $E_{\text{ex}}(\tau) = e^{\tau(A+C)}$, and its expansion is

$$E_{\text{ex}}(\tau) = I + \tau(A + C) + \frac{\tau^2}{2}(A^2 + AC + CA + C^2)$$

$$+ \frac{\tau^3}{6}(A^3 + A^2C + ACA + CA^2 + AC^2 + CAC + C^2A + C^3) + \mathcal{O}(\tau^4). \quad (21)$$

Hence $E_B(\tau) - E_{\text{ex}}(\tau) = -\frac{\tau^2}{2}(AC + CA) + \mathcal{O}(\tau^3)$.

When A and C commute, this is $E_B(\tau) - E_{\text{ex}}(\tau) = -\tau^2 AC + \mathcal{O}(\tau^3)$. This additive update therefore misses the symmetric advection/acoustic cross interaction, which could have significant consequences as will be discussed.

4. Transported acoustic-increment method

The transported-increment modification is motivated by the insight from the above analysis. If the background velocity is frozen at \mathbf{u}_0 , then the frozen linearized Euler equations involve the material derivative

$$(\partial_t + \mathbf{u}_0 \cdot \nabla)\mathbf{W} + C\mathbf{W} = 0,$$

where C denotes the frozen acoustic operator. Thus acoustics propagates relative to a frame moving with \mathbf{u}_0 . Introduce the moving coordinate $\xi \triangleq \mathbf{x} - \mathbf{u}_0 t$. Then

$$(\partial_t + \mathbf{u}_0 \cdot \nabla)\mathbf{W}(\mathbf{x}, t) = \partial_t \widetilde{\mathbf{W}}(\xi, t),$$

so in moving coordinates the frozen system reduces to a pure acoustic evolution. Thus, for constant background conditions, the acoustic evolution computed from data centered at a point P is naturally associated with the material label that started at P , which is located at $P + \mathbf{u}_0 \tau$ at time τ .

To recover the Eulerian value at P , one instead needs information associated with the convective foot

$$P_f \triangleq P - \mathbf{u}_0(P_f)\tau, \quad \text{so that} \quad \mathbf{W}(P, \tau) = e^{\tau C} \mathbf{W}(P_f),$$

under the frozen constant-coefficient model.

An exact frozen acoustic update Note that placing the acoustic disks at the nodes, and limiting the acoustic CFL $c\Delta t/\Delta x \leq 0.5$, allows analytical expressions for the acoustic update because edge-center nodes receive information from two semi-disks in the two adjacent cells (this leads to clean expressions as in Appendix B), while corner nodes receive information symmetrically from four quadrants. This is the geometry illustrated in Figure 1. It is exploited elegantly in the Appendices of Barsukow (2025a): since the disk cuts are always centered on grid lines, the required geometric moments are only half-plane and quadrant moments, and many of these quantities can be precomputed.

When the acoustic disk is not placed at a node, as in the foot-centered variant shown by the red circle in Figure 1, the situation changes substantially. The acoustic center is now the convective foot P_f which is generally an arbitrary point inside a cell. Even under the same acoustic CFL restriction, the disk may cut one vertical and one horizontal grid line at off-center locations. Thus the touched region consists of the cell containing P_f , possibly one neighboring cell in the x -direction, possibly one neighboring cell in the y -direction, and possibly the diagonal cell.

The author was painstakingly able to derive closed-form expressions for this off-center acoustic update by decomposing the disk integrals into three geometric building blocks: full-disk moments, single circular-cap (portion of the acoustic disk cut off by one grid line) moments, and double-cap (portion of the acoustic disk cut off by two grid lines) moments. The usual Barsukow half-plane and quadrant moments are replaced by off-center moments of the reconstructed polynomial data over these cap regions, together with the corresponding radius-derivative and acoustic-history moments required by the pressure and velocity formulas. In the limiting cases where the acoustic center approaches a face midpoint or a corner node, these formulas reduce exactly to the standard Barsukow semi-disk and quadrant updates. Analytical expressions were verified to machine precision using quadrature.

Although this construction gives an exact frozen-acoustic point update centered at the convective foot, it is not computationally attractive in its direct form. The geometry is different for every point value and every time step, so the moments cannot be tabulated once and reused as in the node-centered method. Moreover, each update must dynamically identify the cut cells, translate the local polynomial reconstruction to coordinates centered at P_f , and evaluate the single- and double-cap closed forms. In our implementation, this direct closed-form foot-centered update was approximately 1000× more expensive than the original Barsukow point update, making it useful mainly as an analytical reference rather than as a practical solver component. Even in the linearized Euler regime, this method offered only mild improvements (Refer Table 1 and a mention in the Isentropic vortex test case) at more than 3 orders of magnitude higher cost over a much more effective alternate which follows.

An efficient and accurate alternative We propose a method based on the key insight that, while the split scheme earlier evolves $e^{\tau C} \mathbf{W}(P)$ is *not* the correct Eulerian value at the fixed grid node P at time τ , it **is the exact frozen acoustic evolution associated with the material label that was at P at time 0**, and is therefore naturally associated with the downstream point $P + \mathbf{u}_0 \tau$. The transported-increment method exploits this fact by reconstructing and evaluating the acoustic increment at the foot P_f .

The transported point update is

$$\mathbf{W}_{\text{RB-TAI}}^{n+\tau}(P) \triangleq S_{\text{adv}}(\tau) \mathbf{W}^n(P) + \mathcal{R}_{\Delta}(P_f(P; \tau)), \quad (22)$$

where \mathcal{R}_{Δ} is a \mathcal{Q}_2 reconstruction of the acoustic increment field (see below)

$$\Delta_{\text{ac}}^n(\cdot; \tau) \triangleq S_{\text{ac}}(\tau) \mathbf{W}^n(\cdot) - \mathbf{W}^n(\cdot). \quad (23)$$

The acoustic increment is naturally available at vertices and edge midpoints after the acoustic update. To reconstruct it as a \mathcal{Q}_2 field, one also needs center increments. Therefore the implementation computes an acoustic update of the cell-center primitive node:

$$\mathbf{W}_{c,\text{ac}}^{n+\tau} \triangleq S_{\text{ac}}(\tau) \mathbf{W}_c^n, \quad (24)$$

using the full-circle acoustic operator centered in the cell. Then

$$\Delta_c \triangleq \mathbf{W}_{c,\text{ac}}^{n+\tau} - \mathbf{W}_c^n. \quad (25)$$

Together with the vertex and edge midpoint increments, these center increments define a cellwise \mathcal{Q}_2 reconstruction \mathcal{R}_{Δ} .

Note that density is not an independent acoustic variable in the frozen Euler acoustic subsystem, and therefore its acoustic change must be tied to the pressure change through the invariant $\rho - p/c^2$, otherwise the transported update introduces spurious thermodynamic error at the convective foot. Hence

$$\rho_{\text{ac}}(P_f) = \rho^n(P_f) + \frac{p_{\text{ac}}(P_f) - p^n(P_f)}{c_{P_f}^2}, \quad (26)$$

and therefore the transported acoustic increment used in the point update is

$$\mathcal{R}_{\Delta}(P_f(P; \tau)) = \begin{pmatrix} \Delta p / c_{P_f}^2 \\ \Delta u_{P_f} \\ \Delta v_{P_f} \\ \Delta p_{P_f} \end{pmatrix}. \quad (27)$$

After applying the acoustic evolution operator for a time τ at the vertices and edge midpoints, we obtain

$$\mathbf{W}_{i,j}^{V,\text{ac}}(\tau), \quad \mathbf{W}_{i,j}^{E_v,\text{ac}}(\tau), \quad \mathbf{W}_{i,j}^{E_h,\text{ac}}(\tau).$$

The corresponding acoustic increments are

$$\Delta_{i,j}^V = \mathbf{W}_{i,j}^{V,\text{ac}}(\tau) - \mathbf{W}_{i,j}^V, \quad \Delta_{i,j}^{E_v} = \mathbf{W}_{i,j}^{E_v,\text{ac}}(\tau) - \mathbf{W}_{i,j}^{E_v}, \quad \Delta_{i,j}^{E_h} = \mathbf{W}_{i,j}^{E_h,\text{ac}}(\tau) - \mathbf{W}_{i,j}^{E_h}.$$

These eight boundary increments are not enough to define a \mathcal{Q}_2 polynomial in a cell. A ninth value, the cell-center increment, is also required.

Let $C_{i,j}$ be the Cartesian cell $C_{i,j} = [x_i, x_{i+1}] \times [y_j, y_{j+1}]$, with center $(x_{i+1/2}, y_{j+1/2})$. The primitive center value $\mathbf{W}_{i,j}^C$ is not an independent degree of freedom. It is obtained from the conservative cell average by inverting the two-dimensional Simpson rule.

$$\mathbf{W}_{i,j}^C = \frac{9}{4} \left[\bar{U}_{i,j} - \frac{1}{36} \left(U_{i,j}^V + U_{i+1,j}^V + U_{i,j+1}^V + U_{i+1,j+1}^V \right) - \frac{1}{9} \left(U_{i,j}^{E_h} + U_{i,j+1}^{E_h} + U_{i,j}^{E_v} + U_{i+1,j}^{E_v} \right) \right].$$

The primitive center value is then $W_{i,j}^C = W(U_{i,j}^C) = (\rho_{i,j}^C, u_{i,j}^C, v_{i,j}^C, p_{i,j}^C)^T$. Together with the eight boundary point values, $W_{i,j}^C$ defines the cellwise primitive Q_2 reconstruction $R_{\mathcal{W}}^n$.

This value is not obtained from a conservation constraint, because Δ_{ac} is not a conservative cell-average variable. Instead, it is computed by applying the same locally linearized acoustic evolution operator at the cell center. The acoustic solve at the center freezes $\rho_0 = \rho_{i,j}^C$, $c_0 = c_{i,j}^C$, and evolves the local primitive reconstruction $R_{\mathcal{W}}^n$ by the exact acoustic operator centered at $(x_{i+1/2}, y_{j+1/2})$:

$$\Delta_{i,j}^C = W_{i,j}^{C,ac}(\tau) - W_{i,j}^C.$$

Cellwise Q_2 reconstruction of the acoustic increment. Introduce local reference coordinates on cell $C_{i,j}$:

$$\xi \triangleq \frac{2(x - x_{i+1/2})}{\Delta x}, \quad \eta \triangleq \frac{2(y - y_{j+1/2})}{\Delta y}, \quad (\xi, \eta) \in [-1, 1]^2.$$

Let the one-dimensional quadratic Lagrange basis at nodes $-1, 0, +1$ be

$$\ell_{-}(s) \triangleq \frac{1}{2}s(s-1), \quad \ell_0(s) \triangleq 1-s^2, \quad \ell_{+}(s) \triangleq \frac{1}{2}s(s+1).$$

The cellwise reconstruction of the acoustic increment is the tensor-product interpolant

$$\begin{aligned} R_{\Delta}|_{C_{i,j}}(x, y; \tau) \triangleq & \ell_{-}(\xi)\ell_{-}(\eta) \Delta_{i,j}^V + \ell_0(\xi)\ell_{-}(\eta) \Delta_{i,j}^{E_h} + \ell_{+}(\xi)\ell_{-}(\eta) \Delta_{i+1,j}^V \\ & + \ell_{-}(\xi)\ell_0(\eta) \Delta_{i,j}^{E_v} + \ell_0(\xi)\ell_0(\eta) \Delta_{i,j}^C + \ell_{+}(\xi)\ell_0(\eta) \Delta_{i+1,j}^{E_v} \\ & + \ell_{-}(\xi)\ell_{+}(\eta) \Delta_{i,j+1}^V + \ell_0(\xi)\ell_{+}(\eta) \Delta_{i,j+1}^{E_h} + \ell_{+}(\xi)\ell_{+}(\eta) \Delta_{i+1,j+1}^V. \end{aligned}$$

The transported point update is then evaluated by locating the cell containing the convective foot P_f , computing its local coordinates (ξ_{P_f}, η_{P_f}) , and setting

$$W_{P_f}^{n+\tau}(P) = S_{adv}(\tau)W^n(P) + R_{\Delta}(P_f; \tau).$$

Why the center increment is essential. The eight boundary increments determine the value of R_{Δ} on the cell boundary, but they do not determine the interior Q_2 bubble

$$\ell_0(\xi)\ell_0(\eta) = (1-\xi^2)(1-\eta^2).$$

Changing the center value by an error $e_{i,j}^C$ changes the reconstructed increment by

$$\delta R_{\Delta}(x, y) = \ell_0(\xi)\ell_0(\eta) e_{i,j}^C.$$

This perturbation is invisible on the cell boundary, because $\ell_0(\pm 1) = 0$, but it is maximal at the cell center:

$$\delta R_{\Delta}(x_{i+1/2}, y_{j+1/2}) = e_{i,j}^C.$$

Computing $\Delta_{i,j}^C$ by the same acoustic operator used at the boundary has two important consequences.

First, it makes R_{Δ} a genuine Q_2 interpolation of the acoustic increment field, rather than a boundary-only extension. For a smooth acoustic increment field this gives the usual third-order interpolation accuracy,

$$R_{\Delta}(x, y; \tau) = \Delta_{ac}(x, y; \tau) + O(\Delta x^3 + \Delta y^3).$$

Under hyperbolic scaling $\tau = O(\Delta x) = O(\Delta y)$, this interpolation error is of the same order as the intended Active Flux spatial accuracy.

Second, it preserves constant states. If W^n is uniform, then the exact acoustic evolution returns the same value at vertices, edge midpoints, and cell centers, so $\Delta^V = \Delta^{E_v} = \Delta^{E_h} = \Delta^C = 0$. Therefore $R_{\Delta} \equiv 0$, and the transported update does not create a spurious perturbation.

4.1. Operator split analysis

The transported acoustic-increment update can be written as

$$W^{n+\tau}(P) = S_{\text{adv}}(\tau; W^n)(P) + \Delta_{\text{ac}}^n(P - \tau u^n(P); \tau), \quad (28)$$

where

$$\Delta_{\text{ac}}^n(P_f; \tau) = S_{\text{ac}}(\tau; W^n)(P_f) - W^n(P_f). \quad (29)$$

After linearization about a constant state, the shift $P_f = P - \tau u_0$ is exactly the frozen advection operator $e^{\tau A}$. Thus the acoustic increment is transformed as

$$\Delta_{\text{ac}}(P - \tau u_0; \tau) = e^{\tau A}(e^{\tau C} - I)W^n(P). \quad (30)$$

The advective part contributes $e^{\tau A}W^n(P)$. Hence

$$E_{\text{tr}}(\tau) = e^{\tau A} + e^{\tau A}(e^{\tau C} - I) = e^{\tau A}e^{\tau C}. \quad (31)$$

This is the previously stated equation whose justification was too short. It follows from transporting the acoustic increment, not from re-solving the acoustic equation on a new state.

Since $[A, C] = 0$ in the frozen constant-coefficient model,

$$E_{\text{tr}}(\tau) = e^{\tau A}e^{\tau C} = e^{\tau(A+C)}. \quad (32)$$

Therefore the transported update is not merely a smaller-error split in this model: it is exactly the frozen unsplit advection-acoustic point evolution. In variable-coefficient or fully discrete settings this equality is broken by coefficient variation and interpolation error, but the leading additive cross-term defect is removed.

More generally, without assuming $[A, C] = 0$,

$$E_{\text{tr}}(\tau) - E_{\text{exact}}(\tau) = \frac{\tau^2}{2}(AC - CA) + O(\tau^3) = \frac{\tau^2}{2}[A, C] + O(\tau^3).$$

Thus, the transported Barsukow replaces the additive method's symmetric defect by a commutator defect.

4.2. Mixed wave packet: Numerical results and analysis

To elucidate the characteristics of the above method, we propose a numerical test problem with a uniform subsonic background

$$\rho_0 = 1, \quad p_0 = 1, \quad u_0 = M \cos \phi, \quad v_0 = M \sin \phi,$$

with $M = 0.4$, $\phi = 25^\circ$, and $\gamma = 1.4$. Initialize a sum of independent linearized primitive eigenmodes. The entropy mode has $\rho' = \epsilon_e \cos(k_1 \cdot x)$, $p' = u' = v' = 0$, and the shear mode has $u' = -\epsilon_s \hat{k}_{2,y} \cos(k_2 \cdot x)$, $v' = \epsilon_s \hat{k}_{2,x} \cos(k_2 \cdot x)$, $\rho' = p' = 0$.

The acoustic perturbation is

$$p' = \epsilon \cos(k \cdot x), \quad \rho' = \frac{\epsilon}{c_0^2} \cos(k \cdot x), \quad u' = s \frac{\epsilon}{\rho_0 c_0} \hat{k}_x \cos(k \cdot x), \quad v' = s \frac{\epsilon}{\rho_0 c_0} \hat{k}_y \cos(k \cdot x),$$

where $s = +1$ gives the acoustic-plus branch and $s = -1$ gives the acoustic-minus branch.

The specific packet in the experiment is

$$k_1 = 2\pi(1, 2), \quad k_2 = 2\pi(2, 1), \quad k_3 = 2\pi(3, 2), \quad k_4 = 2\pi(2, 3),$$

with all amplitudes equal to 10^{-6} . For a Fourier wave vector $k = (k_x, k_y)$, define

$$K = |k|, \quad \hat{k} = \frac{k}{K}, \quad \omega_0(k) = u_0 k_x + v_0 k_y.$$

N	Discrete (RB)	rate	Discrete (RB-TAI)	rate	Discrete (RB-Exact)	rate
8	9.134×10^{-7}	–	1.768×10^{-7}	–	1.109×10^{-7}	–
16	2.466×10^{-7}	1.89	2.388×10^{-8}	2.89	1.561×10^{-8}	2.83
32	6.283×10^{-8}	1.97	3.040×10^{-9}	2.97	2.081×10^{-9}	2.91
64	1.578×10^{-8}	1.99	3.817×10^{-10}	2.99	2.632×10^{-10}	2.98
128	3.950×10^{-9}	2.00	4.777×10^{-11}	3.00	3.311×10^{-11}	2.99

Table 1

Maximum error of the baseline Roe–Barsukow method, the transported increment, and the Roe–Barsukow variant with exact convective-foot Mach-disk integration.

The mixed-packet exact linear solution is

$$\begin{aligned}
 W_{\text{ex}}(x, y, t) = & W_0 + \epsilon_e r_e(k_1) \cos(k_1 \cdot x - \omega_0(k_1)t) \\
 & + \epsilon_s r_s(k_2) \cos(k_2 \cdot x - \omega_0(k_2)t) \\
 & + \epsilon_+ r_+(k_3) \cos(k_3 \cdot x - [\omega_0(k_3) + c_0|k_3|] t) \\
 & + \epsilon_- r_-(k_4) \cos(k_4 \cdot x - [\omega_0(k_4) - c_0|k_4|] t).
 \end{aligned}$$

The primitive right eigenvectors are

$$r_e(k) = \begin{pmatrix} 1 \\ 0 \\ 0 \\ 0 \end{pmatrix}, \quad r_s(k) = \begin{pmatrix} 0 \\ -\hat{k}_y \\ \hat{k}_x \\ 0 \end{pmatrix}, \quad r_{\pm}(k) = \begin{pmatrix} 1/c_0^2 \\ \pm \hat{k}_x / (\rho_0 c_0) \\ \pm \hat{k}_y / (\rho_0 c_0) \\ 1 \end{pmatrix}.$$

The time step is tied to the mesh by

$$\Delta t = \frac{0.45h}{c_0}, \quad h = 1/N.$$

The reported error below is the maximum norm over all nodal primitive point values and over all four primitive variables after one step:

$$E_N = \max_{i,j} \max_{\alpha=1,\dots,4} \left| W_{\alpha}^{n+1}(x_i, y_j) - W_{\text{ex},\alpha}(x_i, y_j, \Delta t) \right|.$$

The old node-centered additive update converges at approximately second order in this diagnostic. The transported-increment update converges at third order, and the direct RB-Exact update does not use transported increments. Instead, it directly integrates over the exact Mach disk. This solution also converges at third order. The exact update has a slightly smaller error constant in this test.

Analysis To explain the results, consider a single acoustic branch Fourier mode

$$\mathbf{w}^n(P) = \epsilon r_s(k) e^{ik \cdot P}, \quad s = \pm 1.$$

Let $\alpha = \omega_0(k)\Delta t$, $\beta = sc_0 K \Delta t$. The exact frozen evolution is $\mathbf{w}_{\text{ex}}(P, \Delta t) = \epsilon e^{-i(\alpha+\beta)} r_s(k) e^{ik \cdot P}$. The RB scheme yields

$$\mathbf{w}_B(P, \Delta t) = \epsilon (e^{-i\alpha} + e^{-i\beta} - 1) r_s(k) e^{ik \cdot P}.$$

Subtracting gives

$$\begin{aligned}
 \mathbf{w}_B - \mathbf{w}_{\text{ex}} &= \epsilon [e^{-i\alpha} + e^{-i\beta} - 1 - e^{-i(\alpha+\beta)}] r_s e^{ik \cdot P} \\
 &= \epsilon (e^{-i\alpha} - 1) (1 - e^{-i\beta}) r_s e^{ik \cdot P} \\
 &= \epsilon \omega_0(k) sc_0 K \Delta t^2 r_s e^{ik \cdot P} + \mathcal{O}(\Delta t^3).
 \end{aligned}$$

For any acoustic branch with $\omega_0(k) \neq 0$, $K \neq 0$, and nonzero amplitude, this is a genuine $\mathcal{O}(\Delta t^2)$ one-step defect. Under the hyperbolic scaling $\Delta t = \nu h$, the defect becomes $\mathbf{w}_B - \mathbf{w}_{\text{ex}} = \mathcal{O}(h^2)$.

We now consider the RB-TAI method. Let $A = -(u_0 \partial_x + v_0 \partial_y)I$ be the frozen advection generator and C the frozen acoustic generator. For constant coefficients, A and C commute. The transported increment update with perfect evaluation of the increment is

$$\begin{aligned}\mathbf{w}_{\text{tr}}(P) &= e^{\Delta t A} \mathbf{w}^n(P) + e^{\Delta t A} (e^{\Delta t C} - I) \mathbf{w}^n(P) \\ &= e^{\Delta t A} e^{\Delta t C} \mathbf{w}^n(P).\end{aligned}$$

Since $[A, C] = 0$, $e^{\Delta t A} e^{\Delta t C} = e^{\Delta t(A+C)}$. Thus the transported update has no $\mathcal{O}(\Delta t^2)$ defect in the frozen constant-coefficient model.

For the acoustic Fourier branch, the same statement is just the phase identity $e^{-i\alpha} [1 + e^{-i\beta} - 1] = e^{-i(\alpha+\beta)}$.

Now include the transported Q2 interpolation used in the point-update diagnostic. Let \mathcal{R}_h be the cellwise Q2 interpolant. The transported diagnostic computes

$$\mathbf{w}_{h,\text{f}}(P) = \mathcal{R}_h \mathbf{w}^n(P_f) + \mathcal{R}_h \Delta_{\text{ac}}(P_f),$$

where $\Delta_{\text{ac}} = (e^{\Delta t C} - I) \mathbf{w}^n$. The exact transported value is $\mathbf{w}_{\text{ex}}(P) = \mathbf{w}^n(P_f) + \Delta_{\text{ac}}(P_f)$. Hence $\mathbf{w}_{h,\text{tr}} - \mathbf{w}_{\text{ex}} = (\mathcal{R}_h - I) \mathbf{w}^n(P_f) + (\mathcal{R}_h - I) \Delta_{\text{ac}}(P_f)$. For smooth fixed-wavenumber data, Q2 interpolation gives $(\mathcal{R}_h - I) \mathbf{w}^n = \mathcal{O}(h^3)$. Moreover, $\Delta_{\text{ac}} = (e^{\Delta t C} - I) \mathbf{w}^n = \mathcal{O}(\Delta t)$ for fixed k . Thus $(\mathcal{R}_h - I) \Delta_{\text{ac}} = \mathcal{O}(\Delta t h^3) = \mathcal{O}(h^4)$ under $\Delta t = \mathcal{O}(h)$. Therefore

$$\mathbf{w}_{h,\text{tr}} - \mathbf{w}_{\text{ex}} = \mathcal{O}(h^3).$$

The leading visible error is the Q2 interpolation of the transported state, not the additive advection–acoustics split defect.

5. Numerical Experiments

The previous example showed good performance in the linearized Euler limit. Now, we perform a series of numerical experiments where the non-linearity is important. All tests solve the two-dimensional ideal-gas Euler equations with $\gamma = 1.4$. Cell averages are initialized by quadrature, while active point values are sampled directly from the primitive initial data. In all the experiments the CFL number is defined as $\frac{\Delta t}{\Delta x} (|\mathbf{u}| + c)_{\text{max}}$. No limiters are used in the active flux simulations that follow. For the entropy plots, the mathematical entropy $-\int_A \rho \log \frac{p}{\rho^\gamma} dA$ is used.

5.1. Isentropic vortex.

The domain is $[0, 10] \times [-5, 5]$, with periodic boundary conditions. The vortex is centered initially at $(x_0, y_0) = (5, 0)$ and is convected by the background velocity $(u_\infty, v_\infty) = (1, 0)$. With $\beta = 5$,

$$x_c(t) = x_0 + u_\infty t, \quad y_c(t) = y_0 + v_\infty t,$$

and

$$\delta u = -\frac{\beta}{2\pi} \exp\left(\frac{1-r^2}{2}\right) (y - y_c(t)), \quad \delta v = \frac{\beta}{2\pi} \exp\left(\frac{1-r^2}{2}\right) (x - x_c(t)).$$

The temperature-like variable is $T = 1 - \frac{(\gamma-1)\beta^2}{8\gamma\pi^2} \exp(1-r^2)$, and the primitive state is $\rho = T^{1/(\gamma-1)}$, $u = u_\infty + \delta u$, $v = v_\infty + \delta v$, $p = \rho^\gamma$. A final time of 10 units is taken, which is enough for one periodic pass. The exact solution is thus the same as the initial condition.

The grid-refinement study on the left of Figure 4 confirms that all three schemes are formally third order. The error *constant*, however, is markedly improved by transport. At every resolution the discrete RB-TAI scheme is more accurate than the discrete RB scheme, which in turn is more accurate than the semi-discrete Active Flux. The gap is roughly a factor of three between RB-TAI and the semi-discrete reference. The exact frozen foot update (described in Section 4) was actually found to be slightly less accurate than RB-TAI in this problem (while being more than 3 orders of magnitude more expensive.)

The CFL sweep on the right of Figure 4 is more informative. The semi-discrete scheme loses stability slightly above $\text{CFL} < 0.4$, the discrete RB scheme has a marginally higher stability region. For this problem, the present approach remains stable all the way to $\text{CFL} = 1$. The structural reason is visible already at the level of linearized analysis. In the frozen-velocity setting, where \mathbf{u}_0 is constant, $\mathcal{S}_{\text{adv}}(\tau)\mathbf{W}^n(P) = \mathbf{W}^n(P_f)$, so the transported point update collapses to

$$\mathbf{W}_{\text{TAI}}^{n+\tau}(P) = e^{\tau C} e^{\tau A} \mathbf{W}^n(P). \quad (33)$$

That is, the transported point update is the multiplicative composition of the two subsolvers, whereas the additive RB update is $e^{\tau A} + e^{\tau C} - I$. Both $e^{\tau A}$ and $e^{\tau C}$ are unitary on the linearised Euler system; their product is therefore unitary and more stable than the sum of unitaries. We are careful to remark that the actual operator will not be unitary: the impact of interpolation, nonlinear freezing, primitive-variable point evolution, and conservative cell-average coupling will have to be accounted for. Generally, in every problem that we have evaluated, the present approach is found to be more stable than the discrete RB scheme, yet not as dramatically so as in this problem.

A more striking feature of the right panel of Figure 4 is the U-shape of the RB-TAI error curve. This non-monotone behaviour is reproduced on 16^2 , 32^2 and 64^2 grids (Figure 5), with the optimum drifting only weakly with resolution, indicating that what we are seeing is an intrinsic competition between two distinct error mechanisms in the RB-TAI update, rather than a grid-specific artefact. At high CFL, the dominant contribution is the per-step truncation of the splitting (beyond local linearisation, i.e. the residual non-commutator terms at higher order) together with the foot-point displacement error in the nonlinear advective subsolver. At low CFL, the method takes many small semi-Lagrangian point updates. The accumulated interpolation/reconstruction error of the transported point values can then become visible. The acoustic-increment interpolation error is smaller in the frozen smooth analysis because the increment itself is $O(\tau)$, but nonlinear freezing and repeated primitive-variable reconstruction may produce additional low-CFL accumulation.

The flat error curves of Discrete RB and the semi-discrete scheme do not exhibit this U-shape because their dominant error might be a result of the *additive split* cross-term defect of magnitude $\frac{1}{2}\tau^2(AC + CA)$ per step, which accumulates over $N \sim 1/\tau$ steps to a contribution of order τ in the final time. Once the transport modification removes this dominant defect, the residual reconstruction-accumulation and per-step truncation errors become comparable, and the U-shape emerges clearly. We regard this as a useful diagnostic: the curvature of the RB-TAI error vs. CFL is, in itself, evidence that the leading operator-level defect of the additive split has been suppressed.

5.2. Acoustic Pulse Evolution

This example is adapted from the thesis work of Fan (2017), where the non-linear acoustics equations were considered. Here, we modify the problem (as the original conditions lead to a shock) in the context of the Euler equations. The domain is $[-2.5, 2.5] \times [-2.5, 2.5]$. The initial condition is a Gaussian pulse.

$$\rho = 1 + A \exp(-\alpha r^2), \quad u = 0, \quad v = 0, \quad p = \frac{1}{\gamma} \rho^\gamma.$$

For the nonlinear Euler acoustic pulse runs, we used $\alpha = 20$ and $A = 0.25$. The profiles shown in the comparison plots are taken at $t = 2.5$.

The radial Gaussian pulse is, by construction, an acoustic-only test in its early time evolution: the initial velocity vanishes identically, so the advective subsolver acts only through the small self-induced velocities created by the pulse itself. The test therefore primarily probes the acoustic component of each scheme. Figure 6 shows the converged radial wave structure for RB-TAI at different resolutions. The discrete pulse shape and amplitude approach the analytic reference monotonically, and the wave fronts remain crisply circular at every resolution: a direct visual confirmation that the truly multidimensional acoustic operator of Barsukow and Klingenberg (2022) embedded in the scheme produces no detectable directional bias on the underlying Cartesian grid.

Figure 7 plots the nodal solutions on a radial grid. The coarse-grid solutions display a small amplitude under-prediction and a slight asymmetry across the peak, both of which are systematically reduced under refinement; the four curves collapse onto the reference profile as $\Delta x \rightarrow 0$. It is notable that even at the extremely coarse resolution ($\Delta x = 0.1$), the asymmetry is $< 0.3\%$ and spread over 2 cells!

Figure 8 reports the maximum nodal pressure error (highest resolution is the reference) and the maximum radial asymmetry as a function of Δx . Both appear to converge close to third order. We regard the asymmetry, in particular, as a direct probe of the multidimensional fidelity of the acoustic operator: a dimensionally-split or one-dimensional

Riemann-solver-based scheme would generate $O(1)$ asymmetry on a Cartesian grid through axis-aligned upwinding bias (Barsukow and Klingenberg, 2022), whereas the asymmetries seen here are pure discretisation residue and converge cleanly with the grid.

Figure 9 contrasts the three Active Flux variants on the coarsest grid ($\Delta x = 0.1$). The differences between RB and RB-TAI are small here, as expected: in the absence of significant background advection and at low Mach number, the convective foot P_f remains very close to the Eulerian node P , so the transport modification is almost inert. The semi-discrete solution shows a noticeably broader and more diffusive pulse, reflecting the additional numerical damping. This is consistent with the interpretation of the isentropic vortex test: the principal advantage of the transported discrete scheme over the semi-discrete one lies in the elimination of multistage diffusion and in the multiplicative composition of information transport.

Active Flux with Transported Acoustic Increments

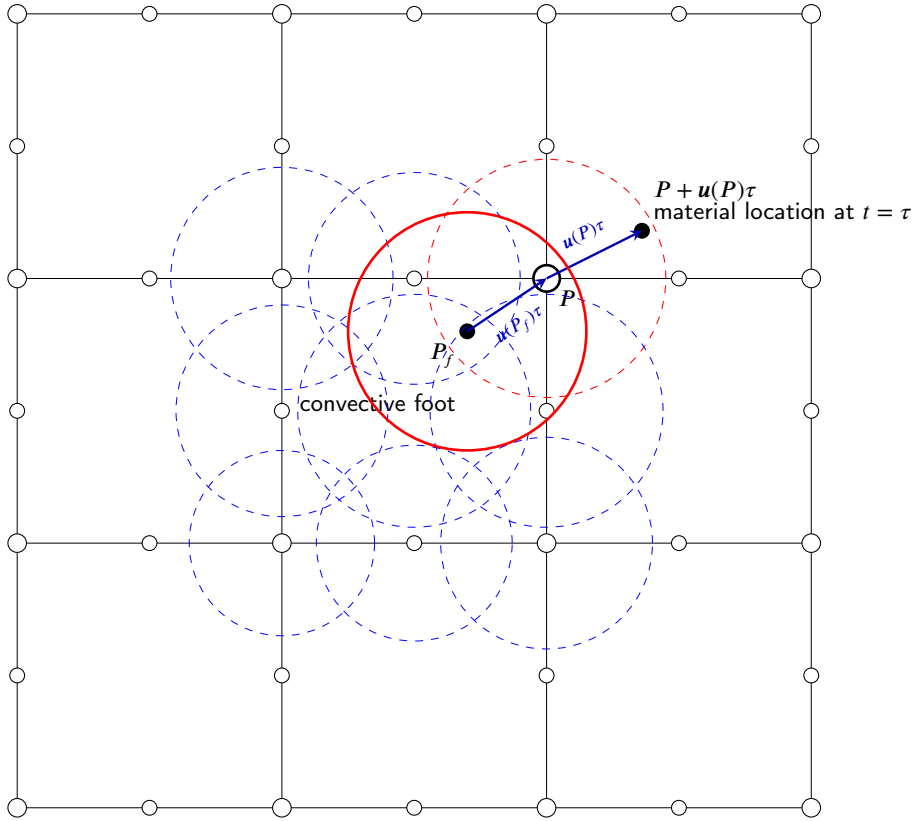


Figure 1: Schematic of the transported-increment. The dashed red circle is the original acoustic disk centered at the grid node P . That acoustic evolution is naturally associated with the material label that started at P , which is located at $P + u_0\tau$ after time τ . To obtain the Eulerian value at the fixed node P at time τ , one instead needs acoustic information associated with the convective foot P_f , represented here by the red circle. This information is obtained by processing transported increments from the dashed circles.

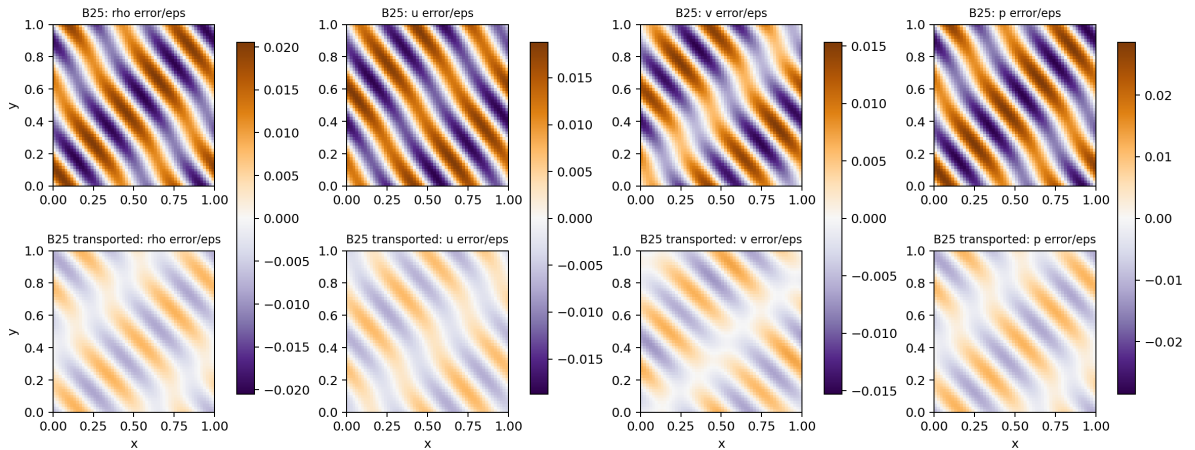


Figure 2: Mixed packet, 56^2 cells: primitive method-minus-exact error contours, scaled by the packet amplitude $\epsilon = 10^{-6}$.

Active Flux with Transported Acoustic Increments

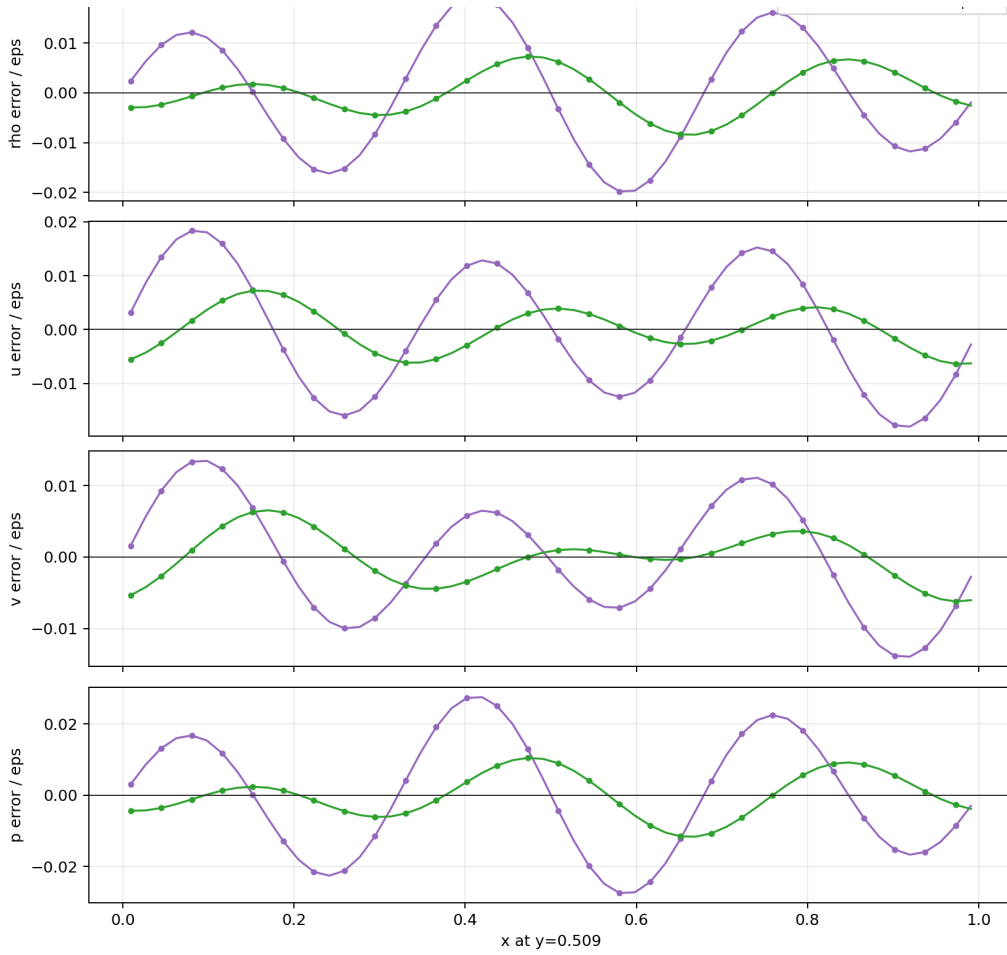


Figure 3: Mixed packet, 56^2 cells: centerline primitive error profiles. Purple: RB, Green: RB-TAI

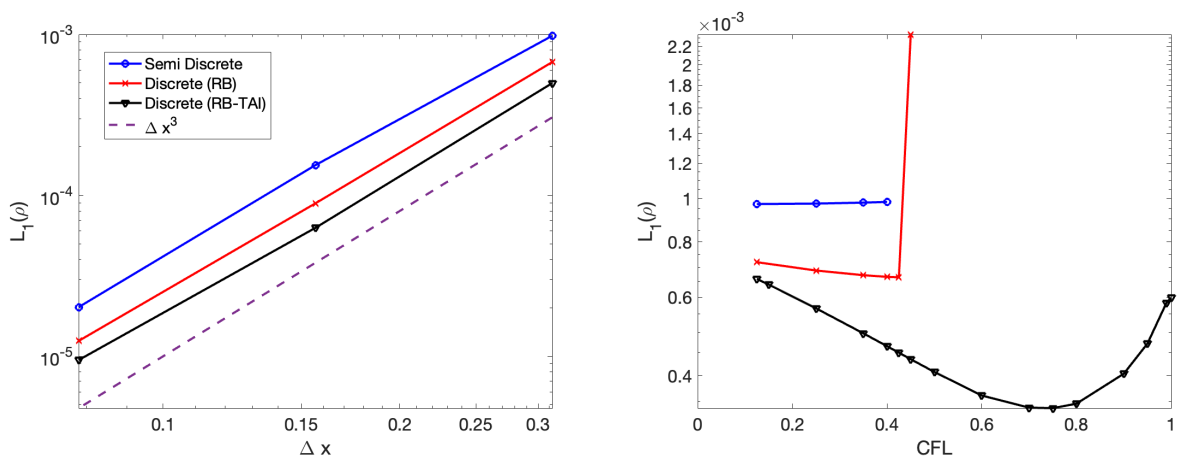


Figure 4: Isentropic vortex convection: Average density error (L_1) after 1 period: 32^2 , 64^2 , 128^2 grids.

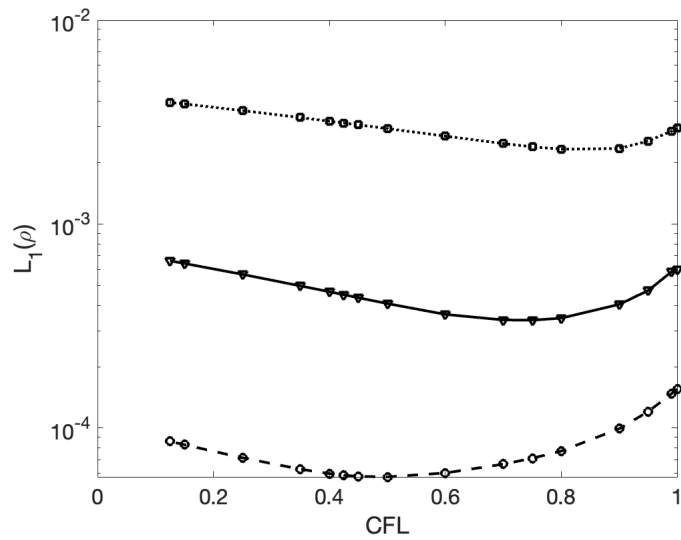


Figure 5: Isentropic vortex convection: Average density error (L_1) after 1 period with transported method: 16^2 , 32^2 , 64^2 grids.

Active Flux with Transported Acoustic Increments

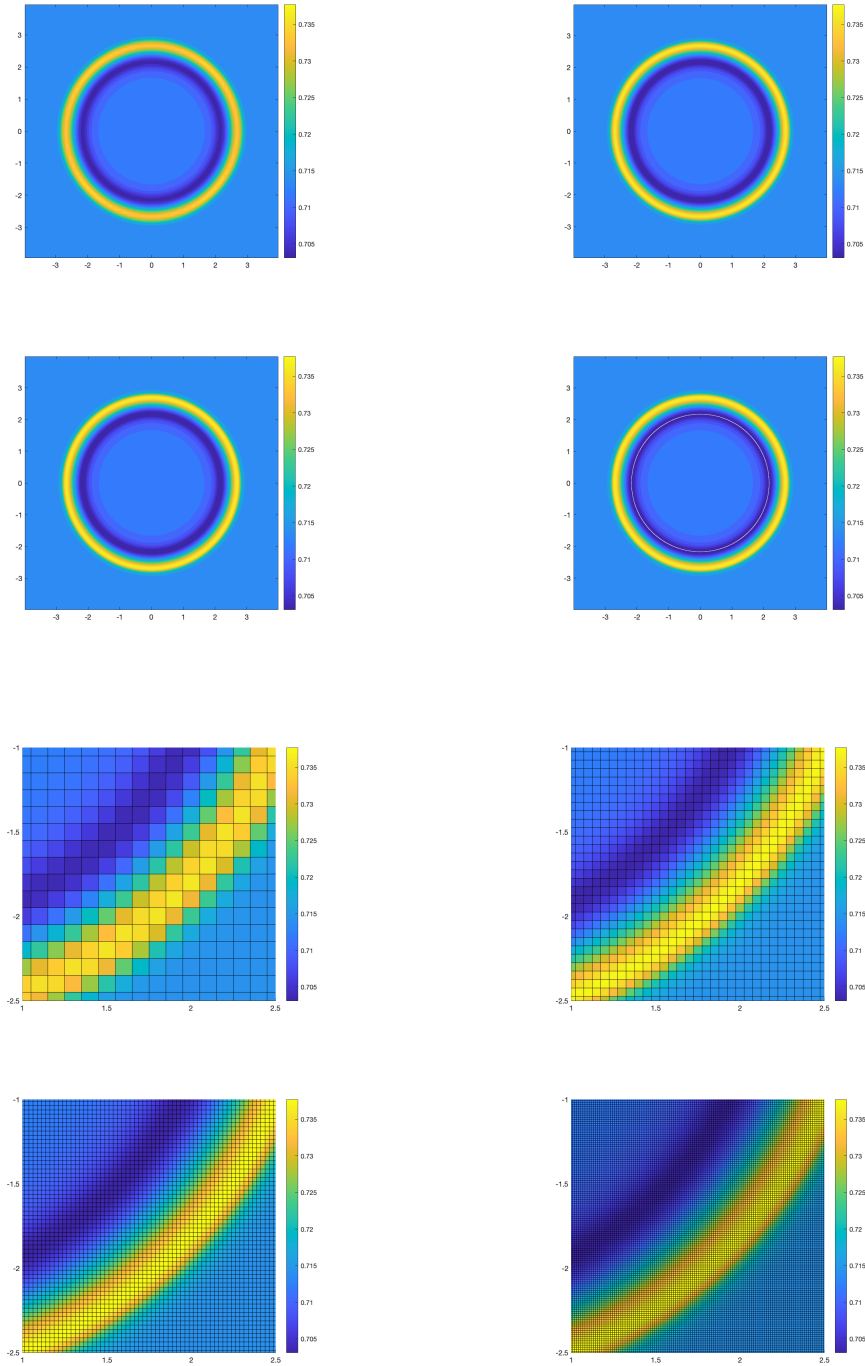


Figure 6: Evolution of Gaussian Pulse at $t=2.5$ at $\Delta x = 0.1, 0.05, 0.025, 0.0125$ with RB-TAI. Cell average values shown.

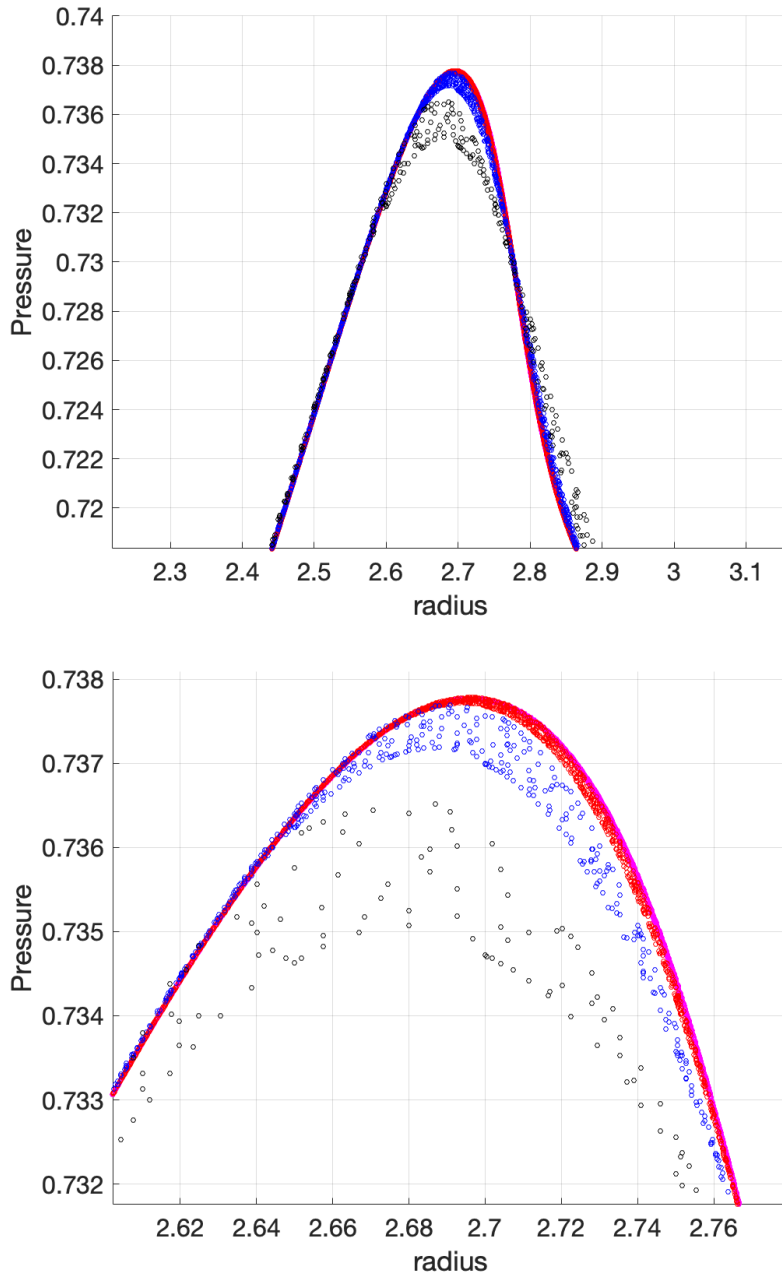


Figure 7: Evolution of Gaussian Pulse at $t=2.5$. Black: $\Delta x = 0.1$; Blue: $\Delta x = 0.05$; Red: $\Delta x = 0.025$; Magenta: $\Delta x = 0.0125$. Nodal values shown.

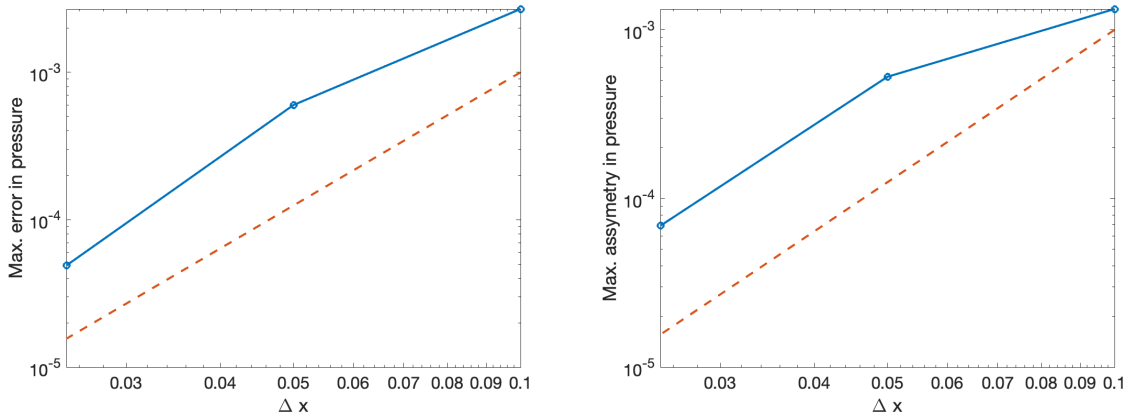


Figure 8: Maximum error and asymmetry in pressure for Gaussian Pulse at $t=2.5$.

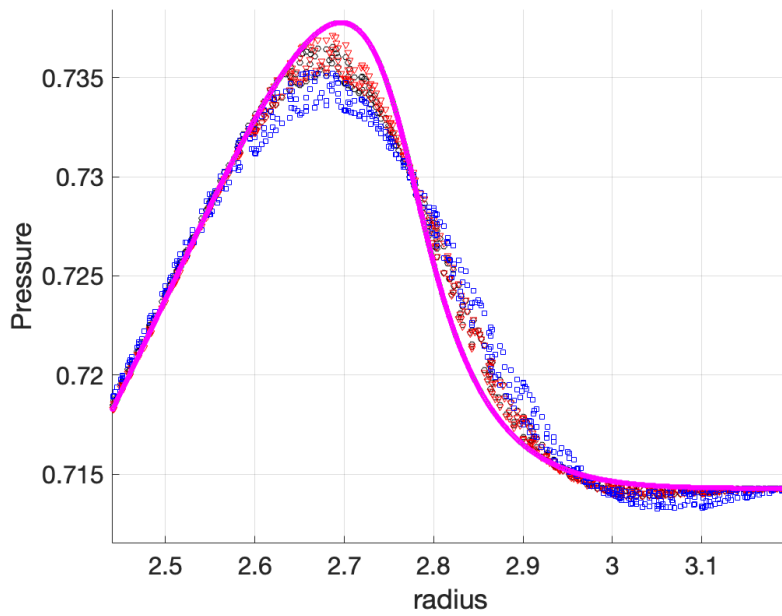


Figure 9: Zoomed in view of Gaussian pulse evolution at $t=2.5$, $\Delta x = 0.1$. Blue: Semi Discrete; Black: Discrete (RB-TAI); Red: Discrete (RB); Magenta: Reference.

Active Flux with Transported Acoustic Increments

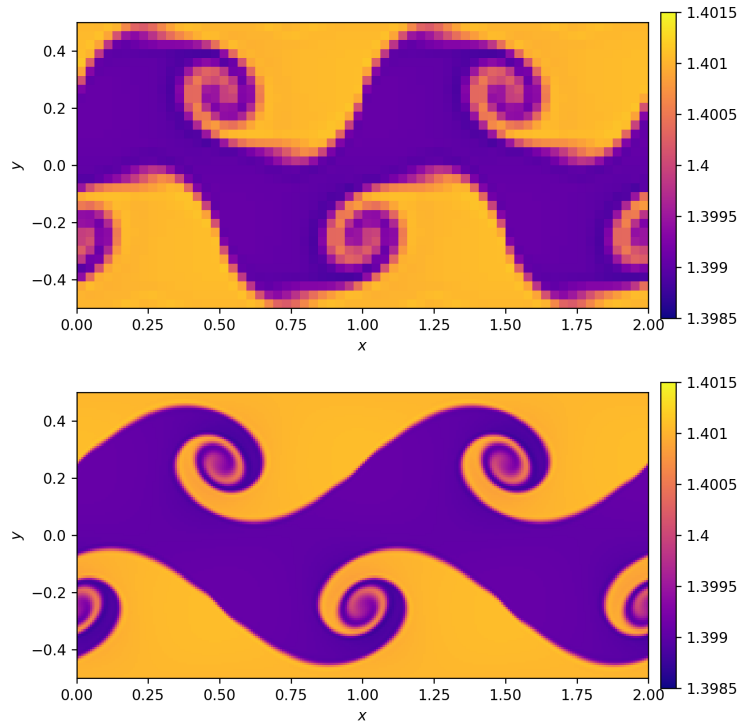


Figure 10: Density contours for shear problem on 64×32 and 256×128 grids using Discrete (RB-TAI)

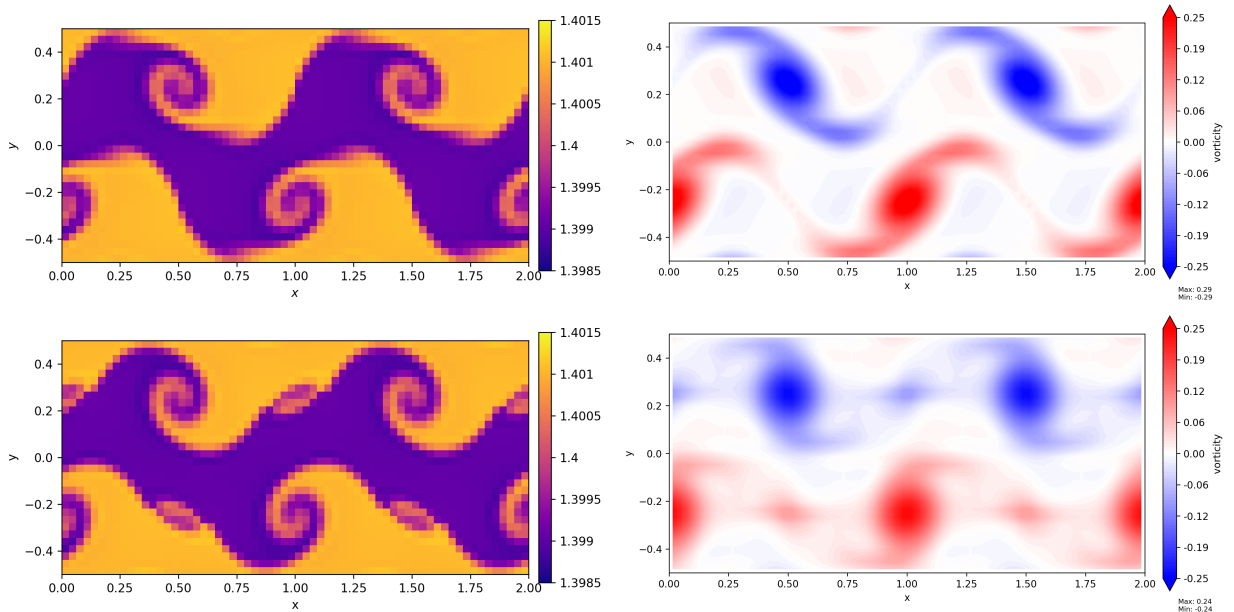


Figure 11: Shear Problem on 64×32 grids. Top: Discrete (RB-TAI), Bottom: DG (P1)

5.3. Low Mach Number Shear

This test case (Abgrall et al., 2025) involves the perturbation of a shear layer. The domain is $[0, 2] \times [-0.5, 0.5]$, with periodic boundary conditions. Define

$$a(y) = \begin{cases} \frac{1}{2} [1 + \sin(16\pi(y + 0.25))], & -9/32 \leq y < -7/32, \\ 1, & -7/32 \leq y < 7/32, \\ \frac{1}{2} [1 - \sin(16\pi(y - 0.25))], & 7/32 \leq y < 9/32, \\ 0, & \text{otherwise.} \end{cases}$$

The primitive initial data are

$$\rho = \gamma + R(1 - 2a(y)), \quad u = M(1 - 2a(y)), \quad v = \delta M \sin(2\pi x), \quad p = 1.$$

Here $R = 10^{-3}$, $M = 10^{-2}$, $\delta = 0.1$. The standard shear-layer visualizations are shown at $t = 80$ in Figure 10. The RB-TAI solution on a very coarse (64×32) mesh appears to track the correct features: primary vortices with a clean wraparound between them, when compared to a refined mesh (256×128) solution; no secondary structures are present. Further confirmation of this reference solution can be seen in Appendix D on higher resolution meshes with a Continuous Galerkin scheme. For this problem, as the Mach number is very small, the difference between the RB and RB-TAI methods was minimal, except for the fact that the RB-TAI was stable up to a CFL number of 0.75, whereas the RB scheme was stable until a CFL number of 0.5. The Semi Discrete method was stable up to a CFL number of 0.3.

Figure 11 reports coarse mesh solutions of the same problem produced by a P1 DG method with the same number of degrees of freedom. The DG solution develops a spurious secondary vortex pair between the primary rollers, accompanied by ringing along the shear interface. These features are possibly artefacts of one-dimensional Riemann-solver-based upwinding and low Mach numbers, where the numerical pressure-velocity coupling can pollute the solution anisotropically (Guillard and Viozat, 1999; Dellacherie, 2010).

The fact that the secondary structures disappear under mesh refinement in the DG and CG methods confirms their non-physical character. More details of the DG and CG method are provided in Appendix D. We are careful to remark that this is *not* meant to be a direct comparison of the accuracy of Active flux vs DG and CG methods. That exercise requires more careful baselining (e.g. (Roe et al., 2018; Barsukow, Klingenberg and Krotsch, 2026; Barsukow, 2025b)), and the present problem is not an ideal test case to evaluate DG methods. Rather the present example reinforces low-Mach number characteristics of Active Flux methods (Barsukow et al., 2019; Barsukow, 2021b) without any adhoc fixes. This test also presents strong evidence that the absence of secondary structure in the coarse-grid results reflects the structure-preserving multidimensional information transport built into the method, rather than a coincidence of resolution.

The vorticity time history (Figure 20 in Appendix D) shows that the symmetric, alternating-sign shear sheets are preserved as coherent structures throughout the run to $t = 80$, with the maximum vorticity drifting only modestly between $t = 20$ and $t = 80$. For a method run at $\mathcal{M} = 10^{-2}$ on a barely-resolved mesh over $\sim 8 \times 10^3$ time steps, this is the structural-preservation behaviour expected of a scheme that propagates the genuine multidimensional acoustic information without preconditioning.

Figure 12 shows a remarkably low level of entropy production even on the coarsest mesh, and also highlights the fact that the discrete active flux technique is less dissipative than the Semi Discrete method. Further, it was confirmed that for all three active flux variants, the integral of vorticity was at machine precision 1×10^{-18} throughout the duration of the simulation, which amounts to 32,000 time steps in the finest mesh, a much desired property in the incompressible limit. The integral of the square of the vorticity, however, does show some decline (Figure 12), with the discrete versions of the method showing smaller declines.

5.4. Robustness test: Compressible, highly unstable Kelvin Helmholtz configuration

The next example involves a compressible and highly unstable shear problem which has been used to stress test high order methods in very recent publications (Glaubitz, Ranocha, Winters, Schlotke-Lakemper, Öffner and Gassner, 2025; Ranocha, Winters, Schlotke-Lakemper, Öffner, Glaubitz and Gassner, 2025; Bercik, Craig Penner and Zingg, 2026). The computational domain is $[-1, 1] \times [-1, 1]$ with periodic boundary conditions. The initial condition is

$$B(y) = \tanh(15y + 7.5) - \tanh(15y - 7.5),$$

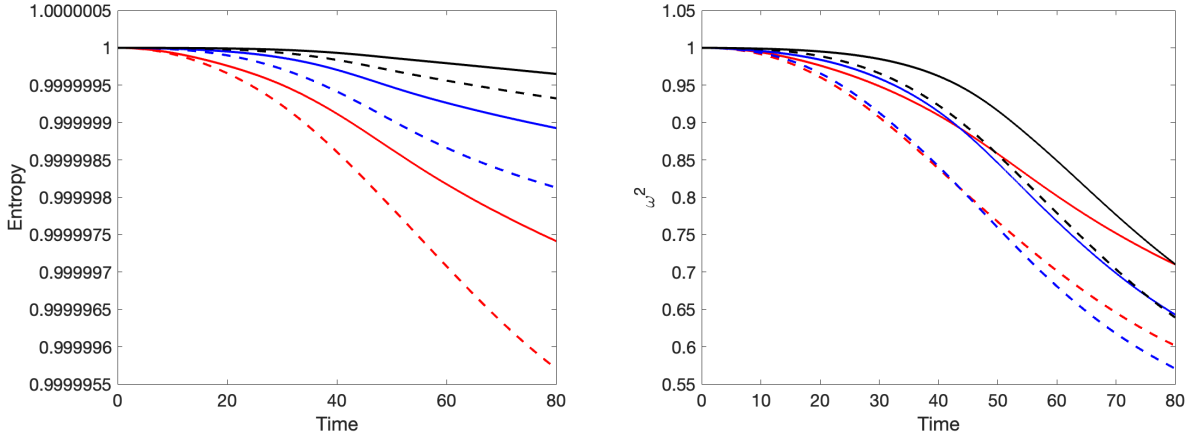


Figure 12: Normalized integral quantities. Red: 64×32 ; Blue: 128×64 ; Black: 256×128 . Solid lines: Discrete (RB-TAI); Dashed lines: Semi Discrete.

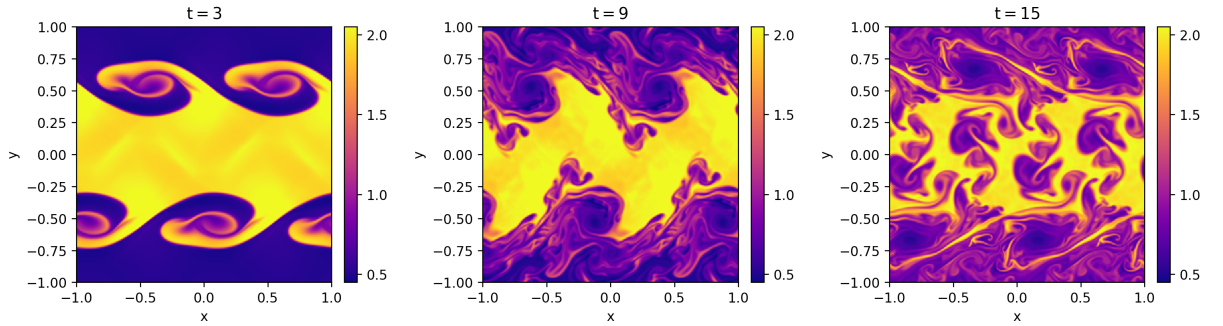


Figure 13: Under-resolved KH problem on 256^2 mesh, Discrete RB-TAI

$$\begin{aligned} \rho(x, y, 0) &= \frac{1}{2} + \frac{3}{4}B(y), & u(x, y, 0) &= \frac{1}{2}(B(y) - 1), \\ v(x, y, 0) &= \frac{1}{10} \sin(2\pi x), & p(x, y, 0) &= 1. \end{aligned}$$

The goal is to evolve the solution to $t = 15$. Most of the numerical methods in the above publications (Glaubitz et al., 2025; Ranocha et al., 2025; Bercik et al., 2026) fail by $t < 5$ units. All three active flux variants spanning under-resolved meshes (64^2 , 128^2 , 256^2) demonstrated robustness.

The Semi Discrete method required a $\text{CFL} < 0.2$, whereas the discrete methods were stable for $\text{CFL} < 0.5$, again with the RB-TAI variant being marginally more stable. In contrast to the prior low Mach number test case, there were noticeable differences between the RB and RB-TAI, as the latter showed noticeably sharper features as can be seen from Figure 15. Further evidence of this is shown in Appendix D.

Figure 14 shows that the entropy production is much more pronounced compared to the nearly incompressible case, giving more credence to the comprehensiveness of the Active Flux method.

6. von Neumann Analysis

This section provides a von Neumann analysis for the vertical face point update. The purpose is to assess the transported increments in the context of a linearized Euler point operator. The base state is uniform,

$$\mathbf{W}_0 = (\rho_0, u_0, v_0, p_0), \quad c_0 = \sqrt{\gamma p_0 / \rho_0}, \quad Z_0 = \rho_0 c_0.$$

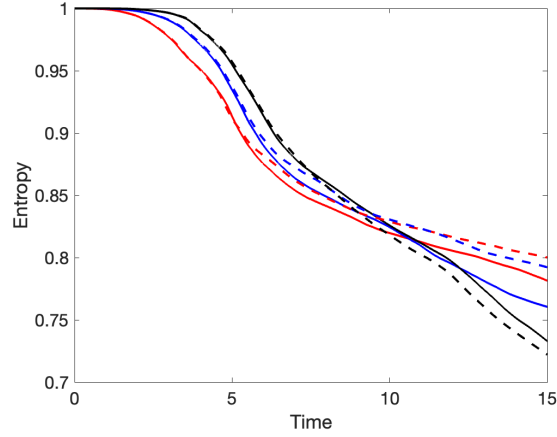


Figure 14: Normalized Entropy. Red: 64^2 ; Blue: 128^2 ; Black: 256^2 . Solid lines: Discrete (RB-TAI); Dashed lines: Semi Discrete.

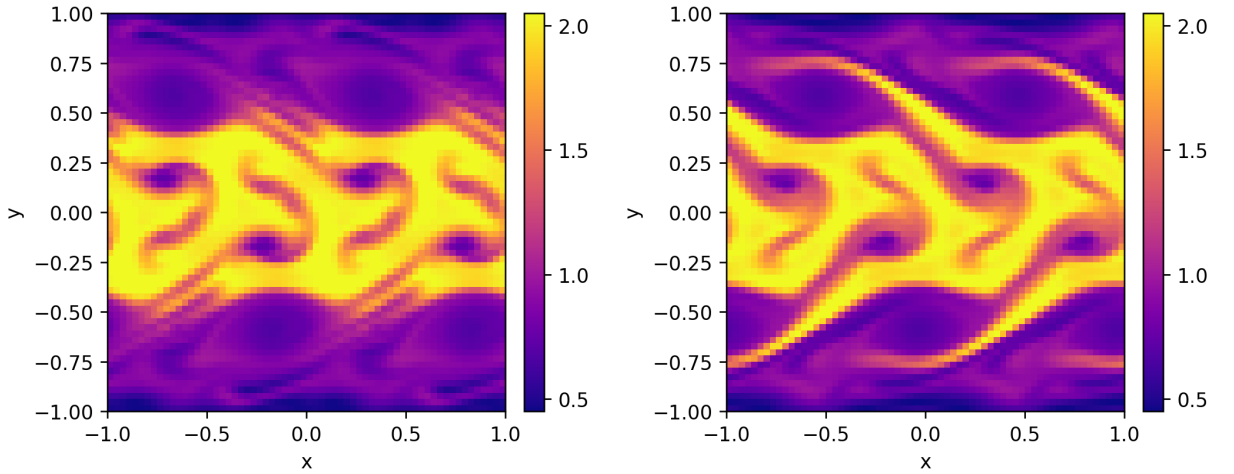


Figure 15: Density contours for under-resolved KH problem on 64^2 mesh. Left: Discrete RB, Right: Discrete RB-TAI

It is possible to write the pressure update in the following form (Appendix B).

$$p_{ac}^{n+1}(P) = P_R + P_L.$$

Set $\xi \triangleq k_x h$, $\eta \triangleq k_y h$, $v \triangleq \frac{c_0 \Delta t}{h}$, $Z_0 \triangleq \rho_0 c_0$. The scalar pressure diagnostic is obtained by substituting a single linearized acoustic Fourier branch. Let

$$\kappa \triangleq Kh = \sqrt{\xi^2 + \eta^2}, \quad \hat{k}_x \triangleq \frac{\xi}{\kappa}, \quad \hat{k}_y \triangleq \frac{\eta}{\kappa},$$

and let $s = -1$ denote the left-running acoustic family and $s = +1$ the right-running acoustic family. Normalize the incoming branch so that its pressure amplitude at P is \hat{p} . The primitive perturbation is then

$$p' = \hat{p} e^{i\mathbf{k} \cdot (\mathbf{x} - P)}, \quad u' = s \frac{\hat{k}_x}{Z_0} \hat{p} e^{i\mathbf{k} \cdot (\mathbf{x} - P)}, \quad v' = s \frac{\hat{k}_y}{Z_0} \hat{p} e^{i\mathbf{k} \cdot (\mathbf{x} - P)}.$$

Therefore the right and left nodal arrays entering Section 3 are

$$P_{rs}^K = \hat{p} \Phi_{rs}^K, \quad U_{rs}^K = s \frac{\hat{k}_x}{Z_0} \hat{p} \Phi_{rs}^K, \quad V_{rs}^K = s \frac{\hat{k}_y}{Z_0} \hat{p} \Phi_{rs}^K, \quad K \in \{R, L\}.$$

Insert these arrays into

$$P_K = Z_0 \langle A_{up}^K, U^K \rangle + Z_0 \langle A_{vp}^K, V^K \rangle + \langle A_{pp}^K, P^K \rangle.$$

The factors Z_0 cancel in the velocity-pressure coupling terms:

$$\frac{P_K}{\hat{p}} = s \hat{k}_x \langle A_{up}^K, \Phi^K \rangle + s \hat{k}_y \langle A_{vp}^K, \Phi^K \rangle + \langle A_{pp}^K, \Phi^K \rangle.$$

Summing the two half-plane contributions gives the single acoustic pressure gain

$$g_{p,ac}^{E_{v,s}}(\xi, \eta, \nu) = \sum_{K \in \{R, L\}} \left[\langle A_{pp}^K, \Phi^K \rangle + s \hat{k}_x \langle A_{up}^K, \Phi^K \rangle + s \hat{k}_y \langle A_{vp}^K, \Phi^K \rangle \right]. \quad (34)$$

Expanding the contractions and collecting conjugate Fourier phases gives a more interpretable form. With $\sigma \triangleq \text{sinc}(\xi/2) \text{sinc}(\eta/2)$, the same scalar can be written as

$$g_{p,ac}^{E_{v,s}} = \mathcal{P}(\xi, \eta, \nu) - i s \left[\hat{k}_x \mathcal{U}(\xi, \eta, \nu) + \hat{k}_y \mathcal{V}(\xi, \eta, \nu) \right]. \quad (35)$$

The real even pressure-pressure part is

$$\begin{aligned} \mathcal{P} = & p_0 + 2p_x \cos \xi + 2p_\sigma \cos(\xi/2) + 2p_y \cos(\eta/2) \\ & + 4p_{xy} \cos \xi \cos(\eta/2) + 4p_{hy} \cos(\xi/2) \cos(\eta/2), \end{aligned}$$

where

$$\begin{aligned} p_0 &= -(\nu - 1)(4\nu^3 - 4\nu^2 - 3\nu + 1), \\ p_x &= -\frac{\nu(2\nu - 1)(2\nu^2 - \nu - 2)}{2}, \\ p_\sigma &= \frac{3\nu\sigma}{2}(4\nu^3 - 6\nu^2 - 3\nu + 3), \\ p_y &= \frac{\nu(4\nu^3 - 10\nu^2 + 9\nu - 1)}{4}, \\ p_{xy} &= \frac{\nu(4\nu^3 - 2\nu^2 + \nu - 1)}{8}, \\ p_{hy} &= -\frac{\nu(4\nu^3 - 6\nu^2 - \nu + 1)}{2}. \end{aligned}$$

The imaginary pressure increment induced by the acoustic velocity components is

$$\begin{aligned} \mathcal{U} &= 4u_{xy} \sin \xi \cos(\eta/2) + 2u_x \sin \xi + 4u_{hy} \sin(\xi/2) \cos(\eta/2) + 2u_\sigma \sin(\xi/2), \\ \mathcal{V} &= 4v_{xy} \cos \xi \sin(\eta/2) + 4v_{hy} \cos(\xi/2) \sin(\eta/2) + 2v_y \sin(\eta/2), \end{aligned}$$

with

$$\begin{aligned} u_{xy} &= \frac{\nu(9\nu^3 - 4\nu^2 + 3\nu - 3)}{24}, & u_x &= -\frac{\nu(9\nu^3 - 8\nu^2 - 9\nu + 6)}{6}, \\ u_{hy} &= -\frac{\nu(3\nu^3 - 4\nu^2 - \nu + 1)}{2}, & u_\sigma &= \frac{3\nu\sigma}{2}(3\nu^3 - 4\nu^2 - 3\nu + 3), \\ v_{xy} &= \frac{\nu^2(4\nu - 3)}{12}, & v_{hy} &= -\frac{\nu^2(2\nu - 3)}{3}, & v_y &= \frac{\nu(4\nu^2 - 9\nu + 6)}{6}. \end{aligned}$$

This collected expression exposes the main symmetries. The pressure-pressure piece is real and even in the wave vector, while the velocity-pressure piece is imaginary and odd through the factors $\sin(\xi/2)$, $\sin \xi$, and $\sin(\eta/2)$. The Simpson center-node correction enters only through the two coefficients p_σ and u_σ .

The exact frozen-acoustic pressure gain for the same branch is $g_{p,\text{ex}}^s(\xi, \eta, \nu) = \exp(-i s \nu \kappa)$. The clean scalar acoustic pressure error is therefore

$$E_{p,\text{ac}}^{E_v,s} = \left| g_{p,\text{ac}}^{E_v,s} - g_{p,\text{ex}}^s \right|. \quad (36)$$

This is also the relative L^2 pressure-profile error for a single Fourier pressure mode. The density has no independent acoustic scalar in this linearized acoustic branch: since

$$\rho_{\text{ac}}^{n+1} = \rho^n + \frac{p_{\text{ac}}^{n+1} - p^n}{c_0^2}, \quad \hat{\rho}^n = \frac{\hat{p}}{c_0^2},$$

the acoustic density gain is the same scalar $g_{p,\text{ac}}^{E_v,s}$. The final additive Barsukow pressure is a different quantity:

$$p^{n+1}(P) = p_{\text{adv}}^{n+1}(P) + p_{\text{ac}}^{n+1}(P) - p^n(P).$$

For a Fourier branch its scalar pressure gain is

$$g_{p,\text{full}}^{E_v,s} = A_{\text{adv}}^{E_v} + g_{p,\text{ac}}^{E_v,s} - 1,$$

and it should be compared with the full Euler phase $\exp\{-i[(u_0 k_x + v_0 k_y) + s c_0 K] \Delta t\}$.

The following plots use the same background as the mixed-wave experiments:

$$\rho_0 = 1, \quad p_0 = 1, \quad (u_0, v_0) = 0.4(\cos 25^\circ, \sin 25^\circ), \quad \gamma = 1.4.$$

the nondimensional wavenumber of the acoustic+ component in the mixed packet. Figure 16 shows the complex-plane locus of the different wave families. In the following slides, we will focus on the acoustic+ family as representative of the underlying mechanics.

Note: For comparison purposes, the vertical-edge semidiscrete generator is used in the following form:

$$M_{\text{SD}}^{E_v}(\mathbf{k}) = - \left[(A^x)^+ D_{x,L}^{E_v}(\mathbf{k}) + (A^x)^- D_{x,R}^{E_v}(\mathbf{k}) + A^y D_y^{E_v}(\mathbf{k}) \right]. \quad (37)$$

Here $D_{x,L}^{E_v}$ is the derivative of the left-cell Q2 reconstruction at the edge, $D_{x,R}^{E_v}$ is the derivative of the right-cell Q2 reconstruction at the edge, and the tangential derivative is the edge-centered difference

$$D_y^{E_v}(\mathbf{k}) = \frac{e^{ik_y h/2} - e^{-ik_y h/2}}{h}.$$

Since the semidiscrete code advances the ODE with SSPRK3, the Discrete (RB) and Discrete (RB-TAI) are compared against the one-step RK3 evolution $\Phi_3(Z) = I + Z + \frac{1}{2}Z^2 + \frac{1}{6}Z^3$, where Z represents the spatial discretization.

Figures 17 and 18 compares the pressure component of a pure $s = +1$ acoustic Fourier input under three point updates. The run uses $\nu = 0.25$, $Kh \in \{0.25, 0.5, 0.75, 1.0\}$. Because this figure includes the convective placement of the acoustic wave, the exact pressure gain is the full convected acoustic phase

$$g_{p,\text{ex}}^+ = \exp\{-i[(u_0 k_x + v_0 k_y) + c_0 K] \Delta t\}.$$

The exact gain now depends on wave-vector angle through $u_0 k_x + v_0 k_y$, and it is clear that the present transported increment approach is the most accurate. Rather surprisingly, the semi-discrete approach is a close second.

Closer to the stability limit, Figure 19, again reinforces the favorable properties of the transported increment approach. In practice, we find that the Discrete (RB-TAI) approach is stable at higher time steps than the Semi-Discrete method.

7. Conclusions and Perspectives

This work introduced a transported acoustic-increment version of the fully discrete multidimensional Active Flux method for the compressible Euler equations. In the additive Roe–Barsukow (Barsukow, 2025a) point update, the acoustic evolution computed at a grid point is added back at that same Eulerian point, although in the presence of background advection that acoustic information is naturally associated with a material label that has moved. Reconstructing the acoustic increment and evaluating it at the convective foot restores this missing transport mechanism without abandoning the compact Active Flux degrees of freedom or the conservative cell-average update. In the frozen linearized setting, the additive update has the form $e^{\tau A} + e^{\tau C} - I$ and misses the symmetric second-order advection–acoustic cross term. The transported-increment update instead gives $e^{\tau A}(e^{\tau C} - I) + e^{\tau A} = e^{\tau A}e^{\tau C}$. Thus, for constant frozen coefficients, where the advective and acoustic generators commute, the transported update reproduces the exact unsplit frozen evolution. More generally, the transported form replaces the additive symmetric defect by a commutator defect, which is the expected residual when the advective and acoustic generators do not commute.

The transported increment exploits the fact that the locally linearized solve still contains valuable information, and thus adds only the reconstruction and evaluation of the acoustic increment at a convective foot, and uses the same conservative space-time Simpson update for cell averages. The cell-center increment is essential in this construction: without it, the Q2 increment field is not determined in the cell interior, and the transported correction would be a boundary extension rather than a genuine Active Flux reconstruction.

The numerical results support this operator-level interpretation across a broad range of tests.

1. In the mixed wave-packet diagnostic, the additive fully discrete point update exhibits the expected second-order one-step defect, while the transported-increment update recovers third-order convergence and approaches the accuracy of a direct convective-foot acoustic update.
2. In the isentropic vortex problem, the transported method retains third-order convergence for the full nonlinear scheme while reducing the error constant relative to both the additive fully discrete method and the semi-discrete Active Flux reference. In the tested vortex configuration, it also remains stable up to total CFL number one, giving an empirical high-CFL behavior consistent with the multiplicative structure of the frozen point update.
3. The acoustic-pulse experiment shows that the transport modification does not degrade the underlying multi-dimensional acoustic propagation. The radial pulse remains symmetric on Cartesian grids, and the measured pressure error and radial-asymmetry error decrease at approximately third order. This is important because the proposed method does not replace the exact locally linearized acoustic operator; it only transports its increment. The symmetry behavior therefore indicates that the transported correction remains compatible with the multidimensional acoustic structure on which Active Flux is built.
4. The low-Mach shear-layer experiment probes a different regime. At $M = 10^{-2}$, the transported method preserves the large-scale coherent shear structures on coarse meshes and avoids the secondary vortex structures observed in DG/CG comparisons. The integral of vorticity remains at machine precision throughout the computation, while the entropy change is minuscule, thus consistent with a nearly incompressible, smooth shear evolution. These results do not constitute a formal all-speed proof, but they indicate that the transported update is compatible with the known low-Mach and vorticity-preserving advantages of multidimensional Active Flux methods.
5. The compressible Kelvin–Helmholtz experiment provides a complementary robustness test. In this highly unstable under-resolved configuration, the Active Flux variants evolve to the target time on meshes as coarse as 64^2 . The discrete methods admit larger time steps than the semi-discrete reference, and the transported variant gives visibly sharper structures in the under-resolved regime. The entropy history shows stronger dissipation than in the low-Mach shear case, as expected for a compressible flow developing fine-scale structure. Thus the entropy behavior is consistent across the two shear tests: nearly conservative in the smooth low-Mach case, and more dissipative in the compressible unstable case.

Several related alternatives were considered. A direct convective-foot acoustic disk integration was derived. This construction is useful as an analytical reference and recovers the standard Barsukow half-plane and quadrant formulas in limiting cases. However, in our prototype, the direct off-center update was several orders of magnitude more expensive than the original point update, while offering only modest accuracy benefits. Midpoint refreezing, direction-dependent acoustic refreezing, and Strang-type compositions are also natural possibilities, but they move the method away from the single-stage, compact, exact-acoustic Active Flux structure. The transported-increment method is therefore best viewed as the minimal correction that captures the missing moving-frame placement of acoustic information while leaving the core Roe–Barsukow infrastructure intact.

Several questions remain open. The present analysis is strongest for the frozen linear point update; a complete theory should include variable coefficients, and the full cell-average/point-value amplification matrix. The present work does not address discontinuous-flow stabilization. All Active Flux computations reported here were performed without limiters or positivity corrections. The compressible Kelvin-Helmholtz calculation is a useful robustness test, but it is not a substitute for shock-capturing evidence. Extending the transported-increment method to flows with shocks, contacts, and near-vacuum states will require nonlinear limiting.

Acknowledgments

This work was supported by Los Alamos National Laboratory under the grant ‘Advanced Algorithms for Multiphysics Analysis’. The author is deeply indebted to the late Professor Phil Roe of the University of Michigan for several discussions on related topics, and ultimately inspiring the ideas that led to this work. This paper is dedicated to his memory.

This work has also benefitted from discussions with Prof. Praveen Chandrasekhar (TIFR, Bangalore), Prof. Christian Klingenberg (Wuerzburg), Ms. Moon Hazarika (U. Michigan), Josh Dolence & Chad Meyer (Los Alamos). Bjorn Kierulf, Eric Johnsen, and Praveen Chandrasekhar provided DG/CG solution comparisons.

OpenAI’s Codex was used for coding and numerical postprocessing, and all outputs were verified multiple times by the author. Scientific content, reasoning, and conclusions are the author’s own.

Appendix

A. Semi-discrete Active Flux

The semi-discrete Active Flux method (Abgrall et al., 2025) is the method-of-lines analogue. One keeps the same degrees of freedom and reconstruction, but evolves the degrees of freedom by an ODE system instead of using a fully discrete evolution operator.

Let

$$Z_h(t) = \{\bar{U}_{ij}(t), \mathbf{W}_{ij}^V(t), \mathbf{W}_{ij}^{E_v}(t), \mathbf{W}_{ij}^{E_h}(t)\}_{i,j} \quad (38)$$

collect all degrees of freedom. The reconstruction operator is denoted by

$$\mathbf{W}_h(\cdot, t) = \mathcal{R}_h Z_h(t). \quad (39)$$

A semi-discrete point update evaluates the right-hand side using derivatives of the reconstruction, or using an equivalent finite-difference formula based on the Active Flux degrees of freedom. In compact notation,

$$\frac{d}{dt} \mathbf{W}_P(t) = \mathcal{L}_{SD}^P(Z_h(t)). \quad (40)$$

For example, using the reconstructed derivative directly gives

$$\mathcal{L}_{SD}^P(Z_h) = - \left(\begin{array}{c} u\rho_x + v\rho_y + \rho(u_x + v_y) \\ uu_x + vu_y + p_x/\rho \\ uv_x + vv_y + p_y/\rho \\ up_x + vp_y + \gamma p(u_x + v_y) \end{array} \right)_{P, \mathbf{W}_h = \mathcal{R}_h Z_h}. \quad (41)$$

At vertices and edge midpoints the derivative of a globally continuous Q_2 reconstruction is not generally single-valued; a semi-discrete implementation must choose a consistent derivative average or a finite-difference residual. This is one reason why the fully discrete evolution-operator form is attractive: the acoustic evolution operator naturally uses the adjacent wedges/half-planes around a point.

The conservative cell average satisfies

$$\frac{d}{dt} \bar{U}_{ij} = -\frac{1}{h} \left(\hat{F}_{i+1,j} - \hat{F}_{i,j} \right) - \frac{1}{h} \left(\hat{G}_{i,j+1} - \hat{G}_{i,j} \right), \quad (42)$$

where the instantaneous edge fluxes are approximated by Simpson quadrature along each edge. For the vertical edge $x = x_i$,

$$\hat{F}_{i,j}(t) = \frac{1}{6}F(W_{i,j}^V) + \frac{4}{6}F(W_{i,j}^{E_v}) + \frac{1}{6}F(W_{i,j+1}^V). \quad (43)$$

The horizontal flux is analogous.

The semi-discrete ODE therefore has the form

$$\frac{d}{dt}Z_h(t) = \mathcal{L}_{SD}(Z_h(t)). \quad (44)$$

In practice this is usually advanced by a Runge–Kutta method, e.g. SSPRK3. This introduces an external time integrator and its own stability/dissipation properties.

B. Explicit Form of Acoustic Update at Vertical edge node

In the active flux solver implementation, the acoustic point value updates are written in the form of monomial coefficients as given by Barsukow (2025a). However, it is possible to write these updates in a more explicit form that also provides more insight into the underlying algorithm, and makes it more amenable to analysis. The update of the point node at the center of the vertical cell face is given as an example in this appendix.

B.1. Right half contribution

Let U^R, V^R, P^R be the right-cell nodal arrays for u, v, p . Set

$$\nu = \frac{\alpha}{h} \triangleq \frac{c_* \Delta t}{h}.$$

The right half-plane acoustic contribution is the direct nodal stencil

$$\begin{aligned} U_R &\triangleq \langle A_{uu}^R, U^R \rangle + \langle A_{uv}^R, V^R \rangle + \frac{1}{Z_*} \langle A_{up}^R, P^R \rangle, \\ V_R &\triangleq \langle A_{uv}^R, U^R \rangle + \langle A_{vv}^R, V^R \rangle + \frac{1}{Z_*} \langle A_{vp}^R, P^R \rangle, \\ P_R &\triangleq Z_* \langle A_{up}^R, U^R \rangle + Z_* \langle A_{vp}^R, V^R \rangle + \langle A_{pp}^R, P^R \rangle. \end{aligned}$$

The right-cell nodal stencils are

$$\begin{aligned} A_{uu}^R &= \begin{bmatrix} \frac{\nu^3(2\nu-3)}{6} & -\frac{4\nu^4-6\nu^3-6\nu^2+9\nu-3}{6} & \frac{\nu^3(2\nu-3)}{6} \\ -\frac{2\nu^3(\nu-1)}{3} & \frac{2\nu(\nu-1)(2\nu^2-3)}{3} & -\frac{2\nu^3(\nu-1)}{3} \\ \frac{\nu^3(2\nu-1)}{6} & -\frac{\nu(2\nu-1)(2\nu^2-3)}{6} & \frac{\nu^3(2\nu-1)}{6} \end{bmatrix}, \\ A_{uv}^R &= \begin{bmatrix} -\frac{\nu(4\nu^2-9\nu+6)}{12} & 0 & \frac{\nu(4\nu^2-9\nu+6)}{12} \\ \frac{\nu^2(2\nu-3)}{3} & 0 & -\frac{\nu^2(2\nu-3)}{3} \\ -\frac{\nu^2(4\nu-3)}{12} & 0 & \frac{\nu^2(4\nu-3)}{12} \end{bmatrix}, \\ A_{up}^R &= \begin{bmatrix} -\frac{\nu^2(\nu-1)^2}{2} & (\nu-1)(2\nu^3-2\nu^2-2\nu+1) & -\frac{\nu^2(\nu-1)^2}{2} \\ \frac{\nu^3(3\nu-4)}{3} & -2\nu(3\nu^3-4\nu^2-3\nu+3) & \frac{\nu^3(3\nu-4)}{3} \\ -\frac{\nu^3(3\nu-2)}{6} & \frac{\nu(6\nu^3-4\nu^2-6\nu+3)}{6} & -\frac{\nu^3(3\nu-2)}{6} \end{bmatrix}, \\ A_{vv}^R &= \begin{bmatrix} \frac{\nu^2(\nu^2-3\nu+3)}{3} & -\frac{4\nu^4-12\nu^3+12\nu^2-3}{3} & \frac{\nu^2(\nu^2-3\nu+3)}{3} \\ -\frac{2\nu^3(\nu-2)}{3} & \frac{4\nu^3(\nu-2)}{3} & -\frac{2\nu^3(\nu-2)}{3} \\ \frac{\nu^3(\nu-1)}{3} & -\frac{2\nu^3(\nu-1)}{3} & \frac{\nu^3(\nu-1)}{3} \end{bmatrix}, \\ A_{vp}^R &= \begin{bmatrix} \frac{\nu(4\nu^2-9\nu+6)}{12} & 0 & -\frac{\nu(4\nu^2-9\nu+6)}{12} \\ -\frac{\nu^2(2\nu-3)}{3} & 0 & \frac{\nu^2(2\nu-3)}{3} \\ \frac{\nu^2(4\nu-3)}{12} & 0 & -\frac{\nu^2(4\nu-3)}{12} \end{bmatrix}, \\ A_{pp}^R &= \begin{bmatrix} \frac{\nu^2(4\nu^2-9\nu+6)}{6} & -\frac{8\nu^4-18\nu^3+6\nu^2+9\nu-3}{6} & \frac{\nu^2(4\nu^2-9\nu+6)}{6} \\ -\frac{2\nu^3(2\nu-3)}{3} & \frac{2\nu(4\nu^3-6\nu^2-3\nu+3)}{3} & -\frac{2\nu^3(2\nu-3)}{3} \\ \frac{\nu^3(4\nu-3)}{6} & -\frac{\nu(8\nu^3-6\nu^2-6\nu+3)}{6} & \frac{\nu^3(4\nu-3)}{6} \end{bmatrix}. \end{aligned}$$

B.2. Left half contribution

Let U^L, V^L, P^L be the left-cell nodal arrays. The left half-plane contribution is

$$\begin{aligned} U_L &= \langle A_{uu}^L, U^L \rangle + \langle A_{uv}^L, V^L \rangle + \frac{1}{Z_*} \langle A_{up}^L, P^L \rangle, \\ V_L &= \langle A_{uv}^L, U^L \rangle + \langle A_{vv}^L, V^L \rangle + \frac{1}{Z_*} \langle A_{vp}^L, P^L \rangle, \\ P_L &= Z_* \langle A_{up}^L, U^L \rangle + Z_* \langle A_{vp}^L, V^L \rangle + \langle A_{pp}^L, P^L \rangle. \end{aligned}$$

The left-cell nodal stencils are

$$\begin{aligned} A_{uu}^L &= \begin{bmatrix} \frac{v^3(2v-1)}{6} & -\frac{v(2v-1)(2v^2-3)}{6} & \frac{v^3(2v-1)}{6} \\ -\frac{2v^3(v-1)}{6} & \frac{2v(v-1)(2v^2-3)}{6} & -\frac{2v^3(v-1)}{6} \\ \frac{v^3(2v-3)}{6} & -\frac{4v^4-6v^3-6v^2+9v-3}{6} & \frac{v^3(2v-3)}{6} \end{bmatrix}, \\ A_{uv}^L &= \begin{bmatrix} \frac{v^2(4v-3)}{12} & 0 & -\frac{v^2(4v-3)}{12} \\ -\frac{v^2(2v-3)}{12} & 0 & \frac{v^2(2v-3)}{12} \\ \frac{v(4v^2-9v+6)}{12} & 0 & -\frac{v(4v^2-9v+6)}{12} \end{bmatrix}, \\ A_{up}^L &= \begin{bmatrix} \frac{v^3(3v-2)}{2} & -\frac{v(6v^3-4v^2-6v+3)}{2} & \frac{v^3(3v-2)}{2} \\ -\frac{v^3(3v-4)}{2} & \frac{2v(3v^3-4v^2-3v+3)}{2} & -\frac{v^3(3v-4)}{2} \\ \frac{v^2(v-1)^2}{2} & -\frac{(v-1)(2v^3-2v^2-2v+1)}{2} & \frac{v^2(v-1)^2}{2} \end{bmatrix}, \\ A_{vv}^L &= \begin{bmatrix} \frac{v^3(v-1)}{3} & -\frac{2v^3(v-1)}{3} & \frac{v^3(v-1)}{3} \\ -\frac{2v^3(v-2)}{3} & \frac{4v^3(v-2)}{3} & -\frac{2v^3(v-2)}{3} \\ \frac{v^2(v^2-3v+3)}{3} & -\frac{4v^4-12v^3+12v^2-3}{6} & \frac{v^2(v^2-3v+3)}{3} \end{bmatrix}, \\ A_{vp}^L &= \begin{bmatrix} \frac{v^2(4v-3)}{12} & 0 & -\frac{v^2(4v-3)}{12} \\ -\frac{v^2(2v-3)}{12} & 0 & \frac{v^2(2v-3)}{12} \\ \frac{v(4v^2-9v+6)}{12} & 0 & -\frac{v(4v^2-9v+6)}{12} \end{bmatrix}, \\ A_{pp}^L &= \begin{bmatrix} \frac{v^3(4v-3)}{6} & -\frac{v(8v^3-6v^2-6v+3)}{6} & \frac{v^3(4v-3)}{6} \\ -\frac{2v^3(2v-3)}{6} & \frac{2v(4v^3-6v^2-3v+3)}{6} & -\frac{2v^3(2v-3)}{6} \\ \frac{v^2(4v^2-9v+6)}{6} & -\frac{8v^4-18v^3+6v^2+9v-3}{6} & \frac{v^2(4v^2-9v+6)}{6} \end{bmatrix}. \end{aligned}$$

The acoustic point value at the vertical face node is

$$u_{ac}^{n+1}(P) = U_R + U_L, \quad v_{ac}^{n+1}(P) = V_R + V_L, \quad p_{ac}^{n+1}(P) = P_R + P_L. \quad (45)$$

The density follows from the frozen acoustic invariant $\rho - p/c_*^2 = \text{constant}$ at the point:

$$\rho_{ac}^{n+1}(P) = \rho_* + \frac{p_{ac}^{n+1}(P) - p_*}{c_*^2}. \quad (46)$$

C. von Neumann analysis quantities

For a cell centered at \mathbf{x}_c , define

$$\sigma(\mathbf{k}) = \text{sinc}\left(\frac{k_x h}{2}\right) \text{sinc}\left(\frac{k_y h}{2}\right), \quad \text{sinc } z = \frac{\sin z}{z}.$$

If \mathbf{x}_q are the four corners and \mathbf{x}_e the four edge midpoints of that cell, the center-node Fourier factor is

$$C_h(\mathbf{k}; \mathbf{x}_c) = \frac{9}{4} \left[\sigma(\mathbf{k}) e^{i\mathbf{k} \cdot \mathbf{x}_c} - \frac{1}{36} \sum_{q=1}^4 e^{i\mathbf{k} \cdot \mathbf{x}_q} - \frac{1}{9} \sum_{e=1}^4 e^{i\mathbf{k} \cdot \mathbf{x}_e} \right]. \quad (47)$$

Relative to the vertical face point P , the right and left phase arrays are

$$\Phi^R = \begin{bmatrix} e^{-i\eta/2} & 1 & e^{i\eta/2} \\ e^{i(\xi-\eta)/2} & C_R & e^{i(\xi+\eta)/2} \\ e^{i(\xi-\eta/2)} & e^{i\xi} & e^{i(\xi+\eta/2)} \end{bmatrix}, \quad \Phi^L = \begin{bmatrix} e^{-i(\xi+\eta/2)} & e^{-i\xi} & e^{i(-\xi+\eta/2)} \\ e^{-i(\xi+\eta)/2} & C_L & e^{i(-\xi+\eta)/2} \\ e^{-i\eta/2} & 1 & e^{i\eta/2} \end{bmatrix}.$$

Here $C_R = C_h(\mathbf{k}; \mathbf{x}_c^R)$ and $C_L = C_h(\mathbf{k}; \mathbf{x}_c^L)$, with the right and left cell centers measured relative to P . Equivalently,

$$C_R = \frac{9}{4} \left[\sigma e^{i\xi/2} - \frac{e^{-i\eta/2} + e^{i\eta/2} + e^{i(\xi-\eta/2)} + e^{i(\xi+\eta/2)}}{36} - \frac{1 + e^{i\xi} + e^{i(\xi-\eta)/2} + e^{i(\xi+\eta)/2}}{9} \right],$$

$$C_L = \frac{9}{4} \left[\sigma e^{-i\xi/2} - \frac{e^{-i(\xi+\eta/2)} + e^{i(-\xi+\eta/2)} + e^{-i\eta/2} + e^{i\eta/2}}{36} - \frac{e^{-i\xi} + 1 + e^{-i(\xi+\eta)/2} + e^{i(-\xi+\eta)/2}}{9} \right].$$

D. Additional details and plots for Shear Problems

This section provides additional context and plots pertaining to the shear problems discussed previously.

The Discontinuous Galerkin method used for comparisons employs a modal basis with $p+1$ Gauss-Legendre quadrature points per dimension. HLLC flux was used between elements and no spatial limiting was used. Time integration was performed using TVD RK3 and a CFL number was set to $0.4/(2p+1)=0.13$. The DG method and the present method have the same number of degrees of freedom for a given mesh.

The Continuous Galerkin method is a spectral element scheme based on summation-by-parts and two point fluxes that ensure additional consistency of Kinetic energy, entropy and internal energy. Additional stabilization is added through gradient jump penalty terms. The results use degree 4 polynomials and classical RK4 method; the grids with cells 32×16 , 64×32 and 128×64 correspond to equivalent AF grids of sizes 128×64 , 256×128 and 512×128 respectively.

References

- Abgrall, R., Barsukow, W., 2023. Extensions of Active Flux to arbitrary order of accuracy. *ESAIM: Mathematical Modelling and Numerical Analysis* 57, 991–1027.
- Abgrall, R., Barsukow, W., Klingenberg, C., 2025. A semi-discrete Active Flux method for the Euler equations on Cartesian grids. *Journal of Scientific Computing* 102, 36.
- Barsukow, W., 2021a. The Active Flux scheme for nonlinear problems. *Journal of Scientific Computing* 86, 1–34.
- Barsukow, W., 2021b. Truly multi-dimensional all-speed schemes for the Euler equations on Cartesian grids. *Journal of Computational Physics* 435, 110216.
- Barsukow, W., 2025a. An Active Flux method for the Euler equations based on the exact acoustic evolution operator. *arXiv:2506.03291*. [arXiv:2506.03291](https://arxiv.org/abs/2506.03291).
- Barsukow, W., 2025b. Semi-discrete active flux as a petrov-galerkin method. *arXiv preprint arXiv:2508.15017*.
- Barsukow, W., Hohm, J., Klingenberg, C., Roe, P.L., 2019. The Active Flux scheme on Cartesian grids and its low Mach number limit. *Journal of Scientific Computing* 81, 594–622.
- Barsukow, W., Klingenberg, C., 2022. Exact solution and a truly multidimensional Godunov scheme for the acoustic equations. *ESAIM: Mathematical Modelling and Numerical Analysis (M2AN)* 56.
- Barsukow, W., Klingenberg, C., Krotsch, S., 2026. On the equivalence of semi-discrete active flux and discontinuous galerkin methods and a comparison of their performance. *arXiv preprint arXiv:2603.18160*.
- Bercik, A., Craig Penner, D.A., Zingg, D.W., 2026. Stable volume dissipation for high-order finite-difference and spectral-element methods with the summation-by-parts property. *Journal of Scientific Computing* 107, 28.
- Chudzik, E., Helzel, C., Lukáčová-Medvid'ová, M., 2024. Active Flux methods for hyperbolic systems using the method of bicharacteristics. *Journal of Scientific Computing* 99, 16.
- Chudzik, E., Helzel, C., Porfetye, A., 2025. A fully discrete truly multidimensional active flux method for the two-dimensional euler equations. *arXiv preprint arXiv:2508.06273*.
- Dellacherie, S., 2010. Analysis of Godunov type schemes applied to the compressible Euler system at low Mach number. *Journal of Computational Physics* 229, 978–1016.
- Eymann, T.A., Roe, P.L., 2011. Active flux schemes for systems, in: 20th AIAA Computational Fluid Dynamics Conference.
- Eymann, T.A., Roe, P.L., 2013. Multidimensional active flux schemes, in: 21st AIAA Computational Fluid Dynamics Conference.
- Fan, D., 2017. On the Acoustic Component of Active Flux Schemes for Nonlinear Hyperbolic Conservation Laws. Ph.D. thesis. University of Michigan.
- Ferrer, E., Rubio, G., Ntoulas, G., Laskowski, W., Marino, O.A., Colombo, S., Mateo-Gabín, A., Marbona, H., de Lara, F.M., Huergo, D., et al., 2023. A high-order discontinuous galerkin solver for flow simulations and multi-physics applications. *Computer Physics Communications* 287, 108700.
- Glaubitz, J., Ranocha, H., Winters, A.R., Schlottke-Lakemper, M., Öffner, P., Gassner, G., 2025. Generalized upwind summation-by-parts operators and their application to nodal discontinuous galerkin methods. *Journal of Computational Physics* 529, 113841.

- Guillard, H., Viozat, C., 1999. On the behaviour of upwind schemes in the low Mach number limit. *Computers & Fluids* 28, 63–86.
- van Leer, B., 1977. Towards the ultimate conservative difference scheme. IV. A new approach to numerical convection. *Journal of Computational Physics* 23, 276–299.
- Maeng, J., 2017. On the Advective Component of Active Flux Schemes for Nonlinear Hyperbolic Conservation Laws. Ph.D. thesis. University of Michigan.
- Mani, M., Dorgan, A.J., 2023. A perspective on the state of aerospace computational fluid dynamics technology. *Annual Review of Fluid Mechanics* 55, 431–457.
- Ranocha, H., Winters, A.R., Schlottke-Lakemper, M., Öffner, P., Glaubitz, J., Gassner, G.J., 2025. On the robustness of high-order upwind summation-by-parts methods for nonlinear conservation laws. *Journal of Computational Physics* 520, 113471.
- Roe, P.L., 2017. Multidimensional upwinding. *Handbook of Numerical Analysis* 18, 53–80.
- Roe, P.L., 2021. Designing CFD methods for bandwidth—a physical approach. *Computers & Fluids* 214, 104774.
- Roe, P.L., 2025. Musings of a computational philosopher, in: Tyacke, J.C., Vadlamani, N.R. (Eds.), *Proceedings of the Cambridge Unsteady Flow Symposium 2024*. Springer Nature Switzerland. doi:10.1007/978-3-031-69035-8_1.
- Roe, P.L., Maeng, J., Fan, D., 2018. Comparing active flux and discontinuous galerkin methods for compressible flow, in: *2018 AIAA aerospace sciences meeting*, p. 0836.
- Wang, Z.J., Fidkowski, K., Abgrall, R., Bassi, F., Caraeni, D., Cary, A., Deconinck, H., Hartmann, R., Hillewaert, K., Huynh, H.T., et al., 2013. High-order cfd methods: current status and perspective. *International Journal for Numerical Methods in Fluids* 72, 811–845.

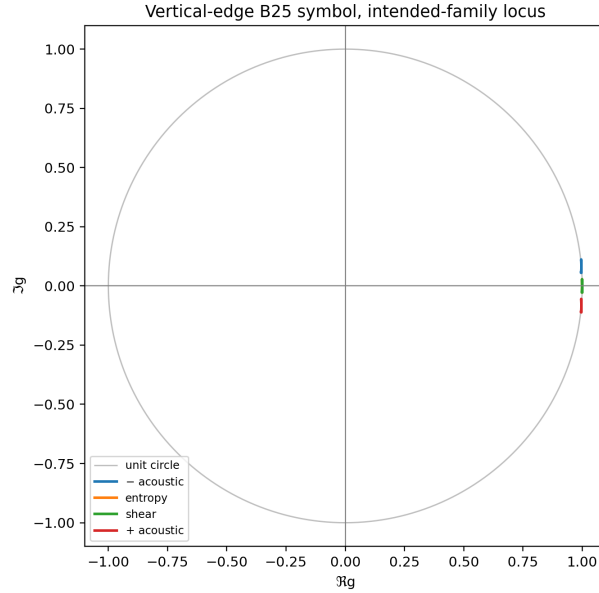


Figure 16: Complex-plane locus of the intended-family vertical-edge symbol G_{jj} as the wave angle varies. Dashed curves are the exact diagonal entries; solid curves are the Discrete (RB) vertical-edge point symbol.

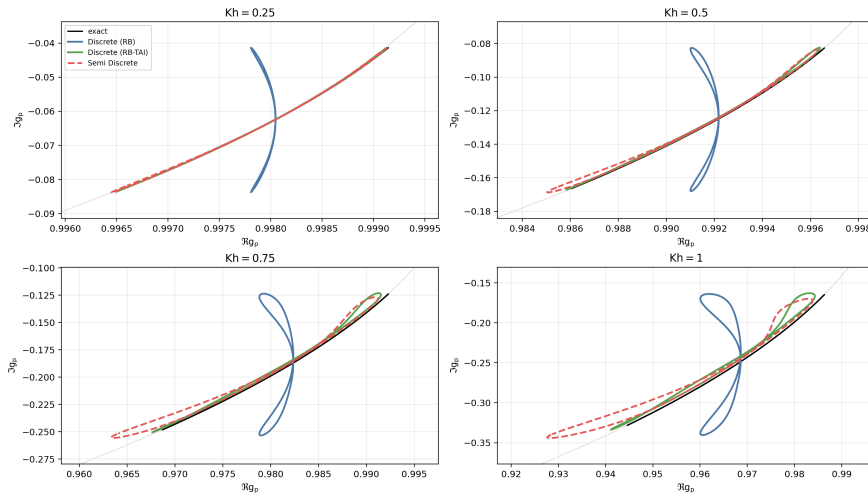


Figure 17: Zoomed complex-plane comparison of the exact convected acoustic pressure gain for a pure $s = +1$ acoustic input for $\nu = 0.25$.

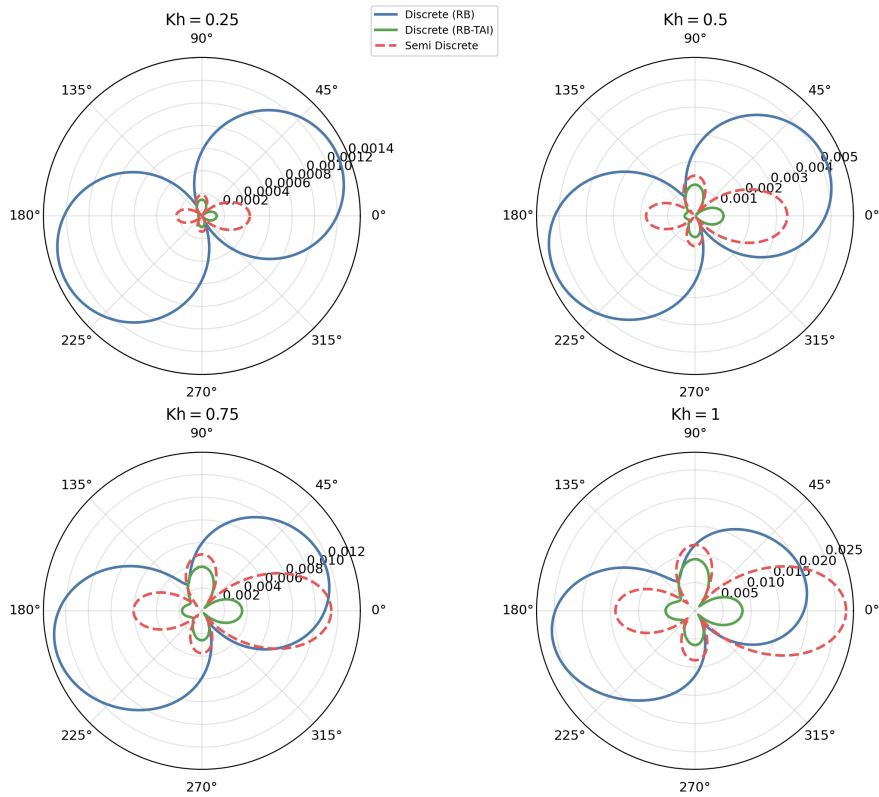


Figure 18: Polar plot of the scalar pressure-gain error as the wave-vector angle is swept at fixed Kh for a pure $s = 1$ acoustic input for $\nu = 0.25$.

Active Flux with Transported Acoustic Increments

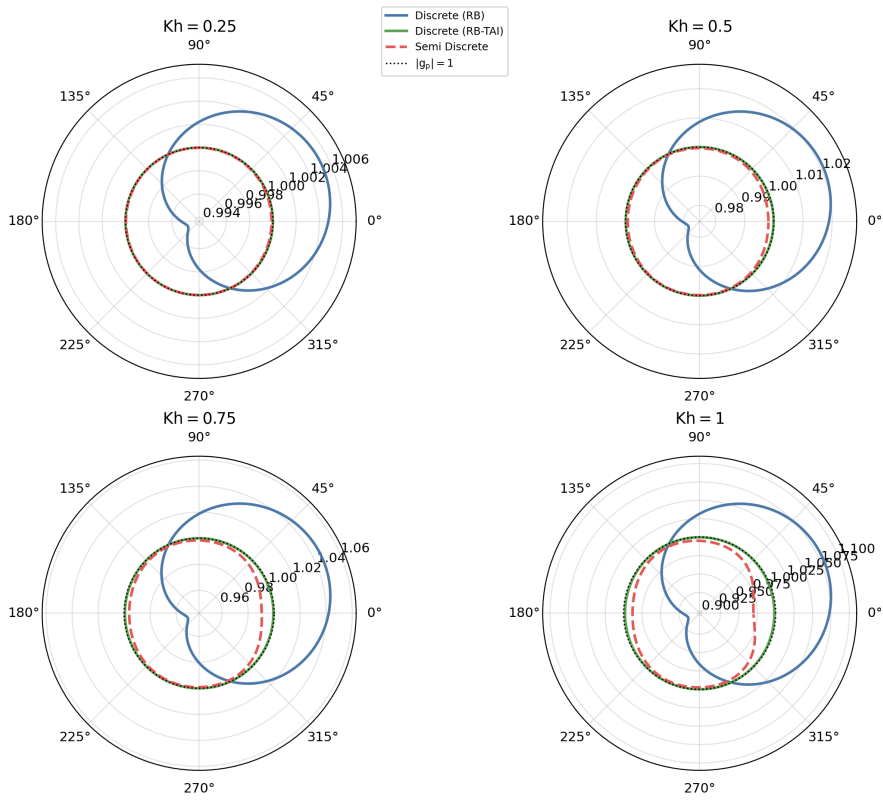


Figure 19: Polar plot of the scalar pressure-gain amplification for a pure $s = 1$ acoustic input for $\nu = 0.5$.

Active Flux with Transported Acoustic Increments

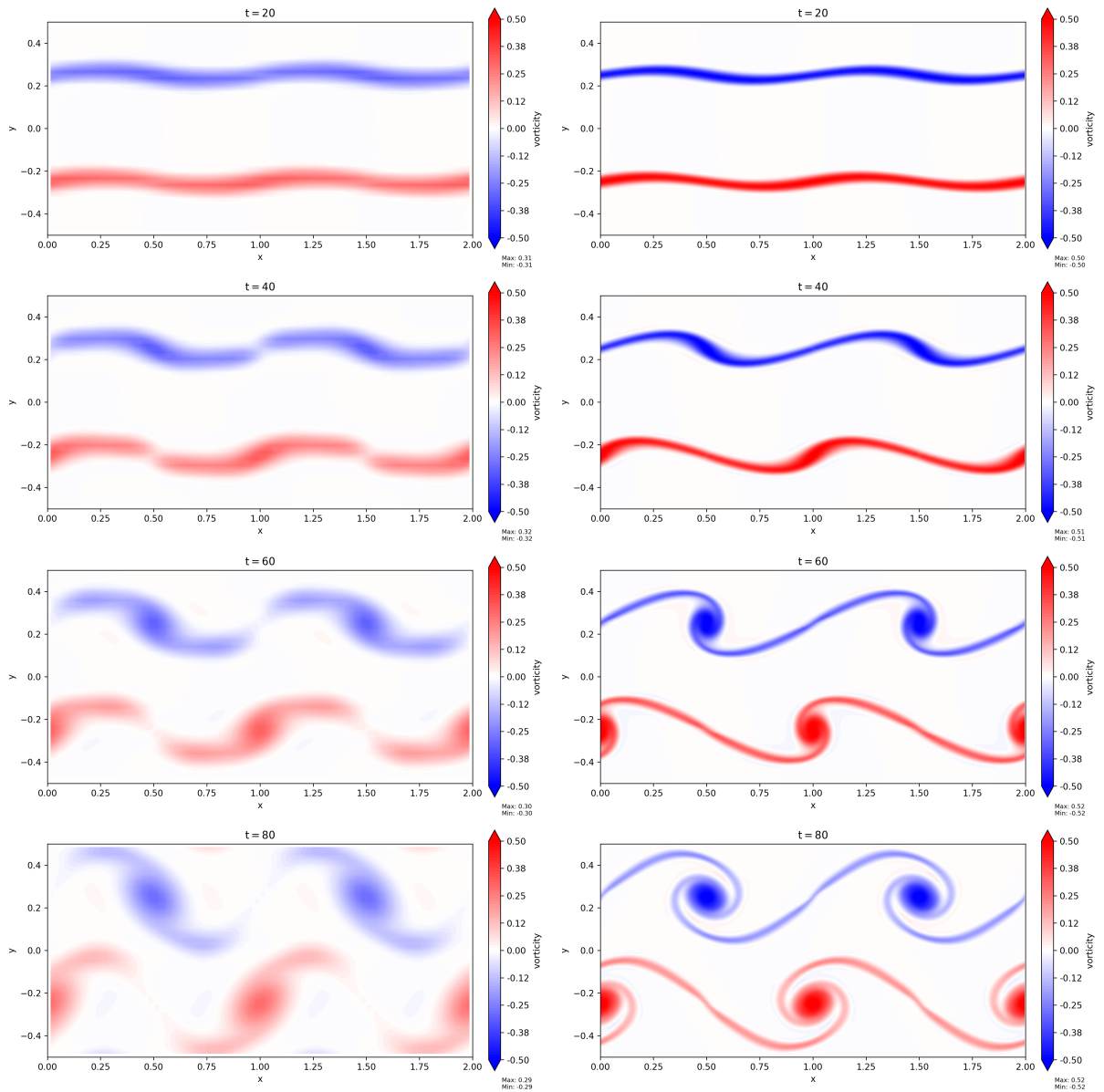


Figure 20: Shear Problem on 64×32 and 256×128 mesh, Discrete (RB-TAI)

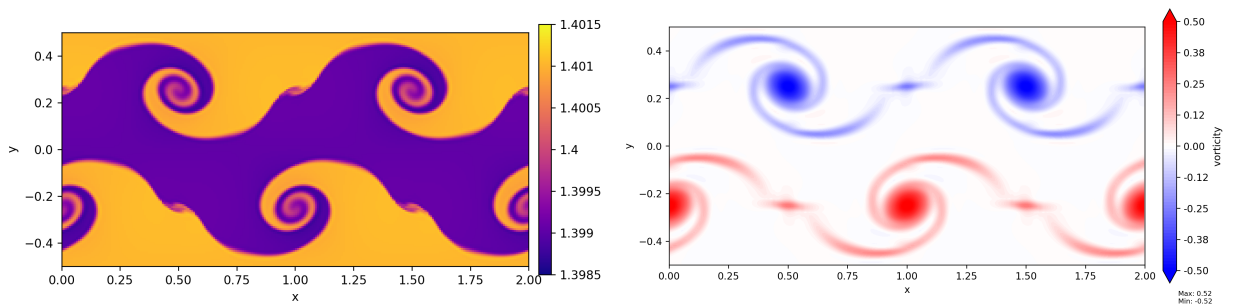


Figure 21: Density and Vorticity contours in shear problem with P1 Discontinuous Galerkin on 256×128 grid.

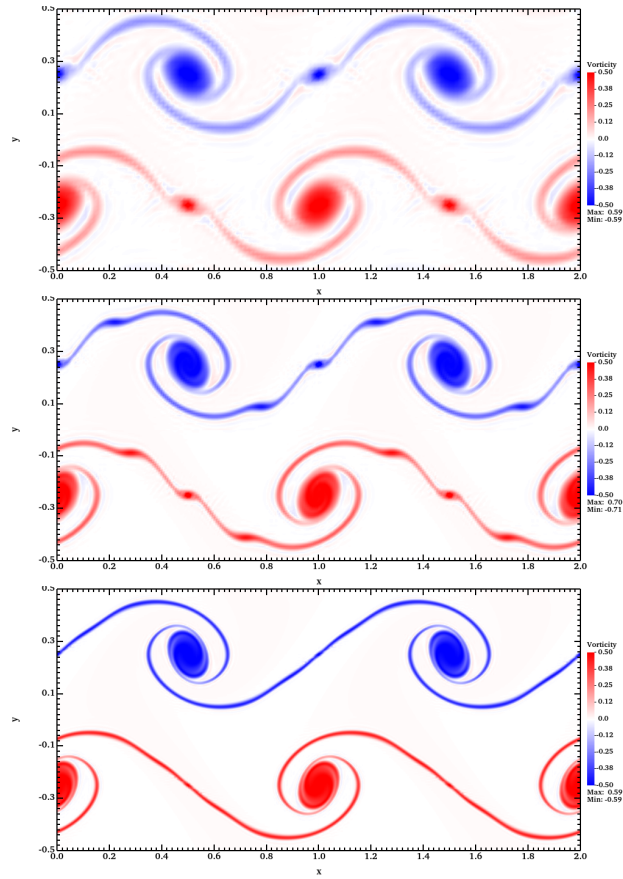


Figure 22: Vorticity contours in shear problem with 5th order Continuous Galerkin: 32×16 ; 64×32 ; 128×64 grids.

Active Flux with Transported Acoustic Increments

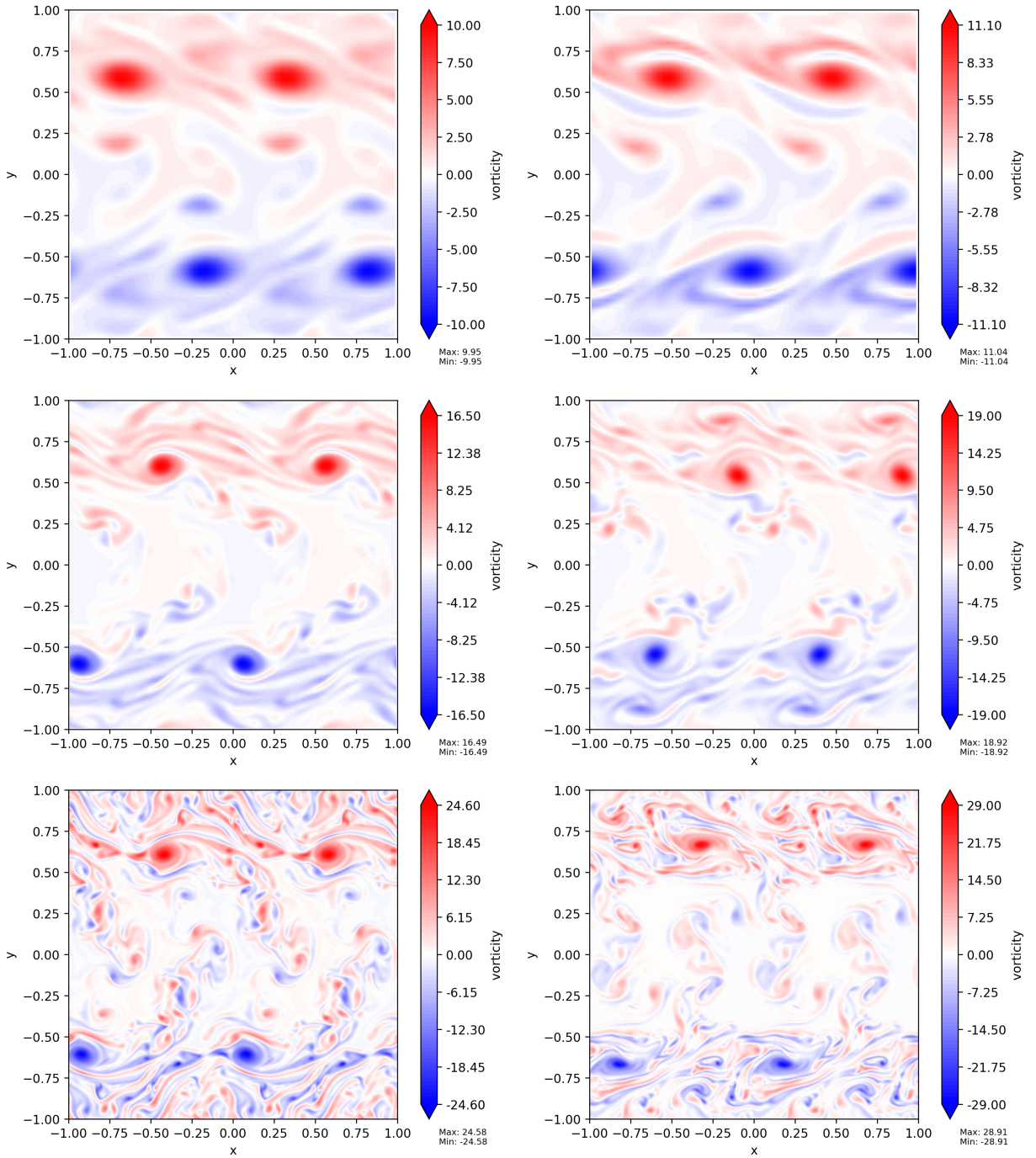


Figure 23: Vorticity contours for under-resolved KH problem. Rows: 64^2 , 128^2 , 256^2 mesh. Columns: Discrete RB, Discrete RB-TAI